University of Bath

Numerical solution of the Giesekus constitutive equation for confined and free surface flows: a finite difference approach

ABSTRACT: This work presents a numerical technique for solving the Giesekus constitutive equation for two-dimensional incompressible flows. The governing equations are approximated by the finite difference method on a staggered grid and solved by second order approximations. The solution of the momentum equations is performed by the implicit Euler method while the Giesekus constitutive equation is resolved by the explicit modified Euler method. It is demonstrated that the methodology employed is capable of dealing with both confined and free surface flows. An analytic solution for fully developed channel flows is presented which is used to verify the numerical technique for channel flows. Mesh refinement studies show the convengence of the methodology in channel flows. The flow through a 4:1 contraction is considered and mesh independence results are provided. This problem is then simulated by a range of Reynolds and Weissenberg numbers and various values of the parameter α. Moreover, the flow produced by a fluid jet flowing onto a rigid surface is simulated. The effect of the parameter α on the flow is investigated.

KEYWORDS: Giesekus model, Finite difference, Analytical solution, Contraction flow, Free surface flow, Jet buckling.

1 Introduction

Numerical solution of viscoelastic flows has been motivated by important industrial flows for example, contraction and cross slot flows, injection molding, filament stretching, container filling, ink jet printers, etc, to mention only a few. These problems do not permit analytic solutions; consequently only numerical solutions can be found. For this reason, numerical methods for predicting Non-Newtonian viscoelastic flows have been a very active research area. The great majority of the techniques developed for simulating viscoelastic flows make use of finite element, finite volume and finite difference methods that employs differential models such as UCM and Oldroyd-B [18, 20–22, 24–27, 30, 31, 36, 41, 86], XPP [8, 19, 28, 32–34], FENE-CR [23, 29, 85], PTT [12–14, 23], Giesekus [4–11, 15–17, 75], among many other. Among these constitutive models, the Giesekus equation has been the subject of work of several investigators. This model is considered to approximate well the rheology of polymers [Giesekus-1985,Giesekus-1982] and has the advantage of simplicity as it involves only two parameters: the time

relaxation λ and the polymer viscosity μ_P. Besides, it can predict first and second normal stress differences. The investigations using this model have concentrated on creeping flows and the results published have consisted mainly in constructing analytic solutions for fully developed flows [10,16,90,91], simulation of contraction flows [6] and flows over a cylinder [92]. Free surface flows have also been tackled by Delvaux and Crochet [5] who presented results of the numerical simulation of two-dimensional delayed die swell and Mu et al. [7] that applied the Giesekus model to predict axisymmetric extrudate swell using a three-dimensional code.

This work is concerned with the numerical solution of the Giesekus model by the finite difference method. We solve the Giesekus equation by the modified Euler method while the momentum equations are computed by the implicit Euler method. We consider confined and moving free surface flows in which the fluid free surface is dealt with the technique presented in Tomé et al. [80]. The developed methodology is verified by using an analytic solution of a channel flow subject to a Newtonian pressure gradient and convergence results are provided by mesh refinement. The complex flow through a 4:1 contraction is investigated and the solutions are compared with the predictions from the finite volume code of Alves et al. [3]. In these results we consider flows with inertia so that the flow through a 4:1 contraction is simulated with Reynolds numbers $Re = 0.1, 1$. Additionaly, we present results of the simulation of a jet flowing onto a rigid plate for several values of the Reynolds and Weissenberg numbers together with a variation of the parameter α. For the problems studied, the parameter α was in the range of $[0, \ 0.5]$.

2   Mathematical formulation

The basic equations governing incompressible flows governed by the Giesekus constitutive equation are the mass conservation and momentum equations together with the Giesekus equation that can be summarized as

$$\nabla \cdot \mathbf{u} = 0, \tag{1}$$

$$\frac{\partial \mathbf{u}}{\partial t} = -\nabla \cdot (\mathbf{u}\mathbf{u}) - \nabla p + \frac{1}{Re}\nabla^2 \mathbf{u} + \nabla \cdot \mathbf{T} + \frac{1}{Fr^2}\mathbf{g}, \tag{2}$$

$$\frac{\partial \boldsymbol{\tau}}{\partial t} = -\nabla \cdot (\mathbf{u}\boldsymbol{\tau}) + (\nabla \mathbf{u})\boldsymbol{\tau} + \boldsymbol{\tau}(\nabla \mathbf{u})^T - \alpha Re\,(\boldsymbol{\tau} \cdot \boldsymbol{\tau})$$

$$-\frac{1}{Wi}\boldsymbol{\tau} + \frac{2}{WiRe}\mathbf{D} \tag{3}$$

where $\mathbf{D} = \frac{1}{2}\big[(\nabla\mathbf{u}) + (\nabla\mathbf{u})^T\big]$ is the rate-of-deformation tensor.

The nondimensional numbers, $Re = \dfrac{\rho U L}{\eta_P}$, $Wi = \dfrac{\lambda U}{L}$, $Fr = \dfrac{U}{\sqrt{g\,L}}$, denote, respectively, the Reynolds,

Weissenberg and Froude numbers. Moreover, U and L are scaling parameters for velocity and lentgh, η_P is the polymeric viscosity, λ is the time relaxation of the polymer and α is the mobility parameter that models the shear thinning behavior of the fluid. We shall investigate flows where $0 \leq \alpha \leq 0.5$.

We point out that, to obtain the momentum equation (2) written in that form, the following EVSS transformation [76]

$$\mathbf{T} = \boldsymbol{\tau} - \frac{2}{Re}\mathbf{D}, \tag{4}$$

was employed. The nondimensionalization of the equations was obtained using the nondimensional variables

$$\mathbf{x}^* = \frac{\mathbf{x}}{L}, \quad \mathbf{u}^* = \frac{\mathbf{u}}{U}, \quad t^* = \frac{U}{L}t, \quad \mathbf{g}^* = \frac{\mathbf{g}}{g} \quad p^* = \frac{p}{\rho U^2}, \quad \boldsymbol{\tau}^* = \frac{\boldsymbol{\tau}}{\rho U^2}, \quad \mathbf{T}^* = \frac{\mathbf{T}}{\rho U^2}.$$

We shall investigate two-dimensional Cartesian flows, so that equations (4), (1), (2) and (3) can be written as:

EVSS equations:

$$T^{xx} = \tau^{xx} - \frac{2}{Re}\frac{\partial u}{\partial x}, \tag{5a}$$

$$T^{xy} = \tau^{xy} - \frac{1}{Re}\Big(\frac{\partial u}{\partial y} + \frac{\partial v}{\partial x}\Big), \tag{5b}$$

$$T^{yy} = \tau^{yy} - \frac{2}{Re}\frac{\partial v}{\partial y}. \tag{5c}$$

Continuity and Momentum equations:

$$\frac{\partial u}{\partial x} + \frac{\partial v}{\partial y} = 0. \tag{6a}$$

$$\frac{\partial u}{\partial t} = -\frac{\partial(u^2)}{\partial x} - \frac{\partial(uv)}{\partial y} - \frac{\partial p}{\partial x} + \frac{1}{Re}\Big(\frac{\partial^2 u}{\partial x^2} + \frac{\partial^2 u}{\partial y^2}\Big)$$
$$+ \frac{\partial T^{xx}}{\partial x} + \frac{\partial T^{xy}}{\partial y} + \frac{1}{Fr^2}g_x, \tag{6b}$$

$$\frac{\partial v}{\partial t} = -\frac{\partial(uv)}{\partial x} - \frac{\partial(v^2)}{\partial y} = -\frac{\partial p}{\partial y} + \frac{1}{Re}\Big(\frac{\partial^2 v}{\partial x^2} + \frac{\partial^2 v}{\partial y^2}\Big)$$
$$+ \frac{\partial T^{xy}}{\partial x} + \frac{\partial T^{yy}}{\partial y} + \frac{1}{Fr^2}g_y. \tag{6c}$$

Giesekus equations:

$$\frac{\partial \tau^{xx}}{\partial t} = \mathcal{G}^{xx}(\mathbf{u}, \boldsymbol{\tau}),$$

$$\mathcal{G}^{xx}(\mathbf{u}, \boldsymbol{\tau}) = 2\Big(\frac{\partial u}{\partial x}\tau^{xx} + \frac{\partial u}{\partial y}\tau^{xy}\Big) - \Big(\frac{\partial(u\tau^{xx})}{\partial x} + \frac{\partial(v\tau^{xx})}{\partial y}\Big)$$

$$- \frac{1}{Wi}\Big\{\tau^{xx} + \alpha\,Re\,Wi[(\tau^{xx})^2 + (\tau^{xy})^2]\Big\} + \frac{2}{Re\,Wi}\frac{\partial u}{\partial x}, \tag{7a}$$

$$\frac{\partial \tau^{xy}}{\partial t} = \mathcal{G}^{xy}(\mathbf{u}, \boldsymbol{\tau}),$$

$$\mathcal{G}^{xy}(\mathbf{u}, \boldsymbol{\tau}) = \frac{\partial u}{\partial x}\tau^{xy} + \frac{\partial u}{\partial y}\tau^{yy} + \frac{\partial v}{\partial x}\tau^{xx} + \frac{\partial v}{\partial y}\tau^{xy} - \Big(\frac{\partial(u\tau^{xy})}{\partial x} + \frac{\partial(v\tau^{xy})}{\partial y}\Big)$$

$$- \frac{1}{Wi}\Big\{\tau^{xy} + \alpha\,Re\,Wi[\tau^{xx}\tau^{xy} + \tau^{xy}\tau^{yy}]\Big\} + \frac{1}{Re\,Wi}\Big(\frac{\partial u}{\partial y} + \frac{\partial v}{\partial x}\Big), \tag{7b}$$

$$\frac{\partial \tau^{yy}}{\partial t} = \mathcal{G}^{yy}(\mathbf{u}, \boldsymbol{\tau}),$$

$$\mathcal{G}^{yy}(\mathbf{u}, \boldsymbol{\tau}) = 2\Big(\frac{\partial v}{\partial x}\tau^{xy} + \frac{\partial v}{\partial y}\tau^{yy}\Big) - \Big(\frac{\partial(u\tau^{yy})}{\partial x} + \frac{\partial(v\tau^{yy})}{\partial y}\Big)$$

$$- \frac{1}{Wi}\Big\{\tau^{yy} + \alpha\,Re\,Wi[(\tau^{xy})^2 + (\tau^{yy})^2]\Big\} + \frac{2}{Re\,Wi}\frac{\partial v}{\partial y}, \tag{7c}$$

2.1   Boundary conditions

To solve equations (6a)-(7c) it is necessary to specify initial and boundary conditions as follows:

Fluid entrance (see $\partial\Omega_2$ in Fig. 1): $\mathbf{u} = \mathbf{U}_{inf}$.

Fluid exits (see $\partial\Omega_3$ in Fig. 1): $\dfrac{\partial \mathbf{u}}{\partial n} = \mathbf{0}$, where n denotes the normal direction to the boundary.

Rigid boundaries: u=0 (see $\partial\Omega_3$ in Fig. 1).

Free surface (see $\partial\Omega_4$ in Fig. 1): A free surface is an interface between air and viscous fluid. It is supposed that surface tension forces can be neglected in which case, the boundary conditions on the free surface can be represented as

$$\boldsymbol{\sigma} \cdot \mathbf{n} = \mathbf{0}, \tag{8}$$

where $\boldsymbol{\sigma} = -p\mathbf{I} + \dfrac{2}{Re}\mathbf{D} + \mathbf{T}$ is the total stress tensor and $\mathbf{n}$ is the vector normal to the interface. For two-dimensional surfaces, one can take $\mathbf{n} = (n_x, n_y)$ and $\mathbf{m} = (n_y, -n_x)$ so that condition

(8) can be represented by equations

$$p = n_x^2 T^{xx} + n_y^2 T^{yy} + 2n_x n_y T^{xy} + \frac{2}{Re}\Big[n_x^2 \frac{\partial u}{\partial x} + n_y^2 \frac{\partial v}{\partial y} + n_x n_y \Big(\frac{\partial u}{\partial y} + \frac{\partial v}{\partial x}\Big)\Big], \qquad (9a)$$

$$\Big[2n_x n_y \Big(\frac{\partial u}{\partial x} - \frac{\partial v}{\partial y}\Big) + (n_y^2 - n_x^2)\Big(\frac{\partial u}{\partial y} + \frac{\partial v}{\partial x}\Big)\Big] =$$
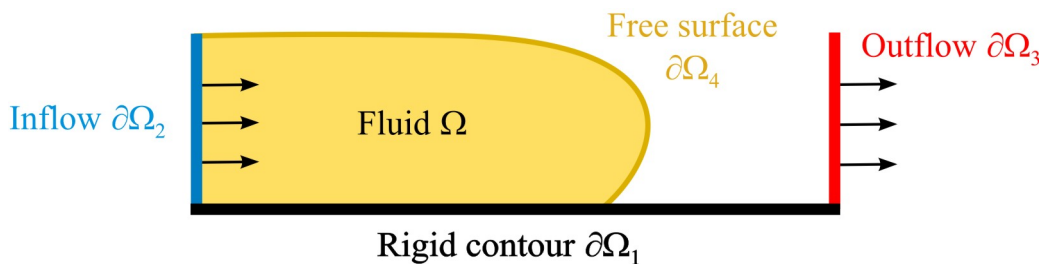$$-Re\Big[n_x n_y (T^{xx} - T^{yy}) + (n_y^2 - n_x^2)T^{xy}\Big]. \qquad (9b)$$

Figure 1: Types of boundaries considered.

3   Numerical method

The equations presented in Section 2 are solved using an updated Marker-and-Cell method introduced by Tomé et al. [77, 80] and the implicit technique of Oishi et al. [28], that employs a finite difference method on a staggered grid (see Fig. 2a. for the positions of variables in a cell). We are interested in flows that possess a moving free surface so a strategy to define the fluid contour, thus the free surface, is employed. This technique is presented in detail by Tomé et al. [80], in which the free surface is described by a set of particles that moves with the local fluid velocity (see Fig. 3a). The fluid body is represented by the volume encapsulated by the closed surface obtained by connecting these particles (see Fig. 3b).
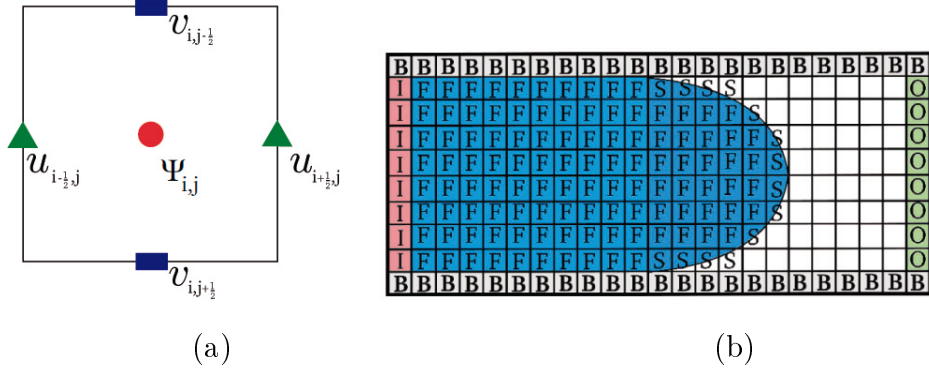
Figure 2: (a) Description of cell employed in the mesh. The variables related to pressure and the stress tensor positioned at cell centre and denoted by Ψ; (b) Type of cells considered.

Figure 3b illustrates the representation of the fluid using this technique. However, to implement this technique it is necessary that the cells within the mesh are defined into several groups of cells as follows:

Rigid boundary (B): these cells define the position and location of rigid conotours.

Inflow boundary (I): cells that model 'fluid entrances' ('inflows')

Outflow boundary (O): cells that define 'fluid exits' ('outflows')

Empty cells (E: cells that do not contain fluid

Full cells (F): cells contain fluid and has no contact with **E**-faces

Surface cells (S): cells contain fluid and has at least one face in contact with **E**-faces
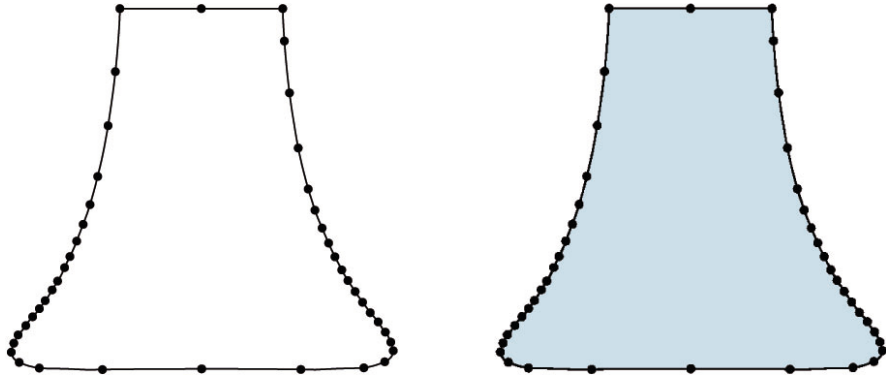
(a) Representation of fluid free surface.　　　　(b) Volume of fluid represented.

Figure 3: Fluid representation.

Due to incompressiblity, equations (1)-(2) must be solved simultaneously which couples the velocity and pressure fields. There are numerical methods that solve the coupled system of equations to obtain the solutions. However, the associated non-linearities make these methods to have computational difficulties to converge which lead them not to be robust. To avoid the complications that arise to solve the coupled system, several strategies do uncouple the velocity and pressure fields have been developed. In this work, the solution of the system of equations (1)-(2) is computed by the projection method proposed by Chorin [62, 63]. This method is based on the Theorem of Decomposition of Helmholtz-Hodge (TDHH) [70] which is also known as the Ladyzhenskaja theorem [72], which is presented next.

(**Decomposition of Helmholtz-Hodge**): Let Ω be a region having a smooth boundary $\partial\Omega$ and $\widetilde{\mathbf{u}}$ a vector field defined on Ω. Then, $\widetilde{\mathbf{u}}$ can be decomposed in a unique form as

$$\widetilde{\mathbf{u}} = \mathbf{u} + \nabla\psi \tag{10}$$

where ψ is a scalar function defined on Ω. The vector field $\mathbf{u}$ is solenoidal and is parallel to $\partial\Omega$, namely,

$$\nabla \cdot \mathbf{u} = 0, \quad \text{and} \quad \mathbf{u} \cdot \vec{n} = 0, \tag{11}$$

where $\vec{n}$ is a normal unit vector that points to the exterior of $\partial\Omega$.

We make use of this theorem and compute the solutions of equations (1)-(7c) in two steps: in the first step, $\boldsymbol{\tau}(\mathbf{x}, t_n)$ is used to compute the velocity $\mathbf{u}(\mathbf{x}, t_{n+1})$ and the pressure $p(\mathbf{x}, t_{n+1})$ at time t_{n+1}; in the next step, the new fields of velocity and pressure are employed to calculate $\boldsymbol{\tau}(\mathbf{x}, t_{n+1})$.

Equation (6a) together with equations (6b) and (6c) are the same as those employed to simulate flows of a XPP fluid [28] and are solved by an implicit procedure that resolves a linear system to obtain a tentative velocity field, followed by the solution of a Poisson equation to ensure incompressibility throughout. One feature of the solution of the Poisson equation is that it is coupled with the pressure condition on the free surface (9a) through the incompressibility condition to calculate the pressure on the free surface. This methodology is described in detail in the work of Oishi et al. [28] and therefore it will not be presented here.

The focus of this work is the solution of the Giesekus model. First we present the numerical method for solving the Giesekus constitutive equation and, with the purpose of verification of the resulting computer solver, apply it to simulate flows in a channel and 4:1 contraction. Then, we investigate its application to free surface flows governed by the Giesekus model.

3.1   Solution of the Giesekus constitutive equation

The tensor $\boldsymbol{\tau}(\mathbf{x}, t_{n+1})$ is calculated by the explicit modified Euler method which is second order in time. Therefore, the components of $\boldsymbol{\tau}(\mathbf{x}, t_{n+1})$ are obtained in two steps as follows.

1. Step 1: Calculate $\overline{\tau^{xx}}(\mathbf{x}, t_{n+1})$, $\overline{\tau^{xy}}(\mathbf{x}, t_{n+1})$, $\overline{\tau^{yy}}(\mathbf{x}, t_{n+1})$, by

$$\overline{\tau^{xx}}(\mathbf{x}, t_{n+1}) = \tau^{xx}(\mathbf{x}, t_n) + \delta t \mathcal{G}^{xx}(\mathbf{u}^{(n+1)}, \boldsymbol{\tau}(\mathbf{x}, t_n)), \tag{12}$$

$$\overline{\tau^{yy}}(\mathbf{x}, t_{n+1}) = \tau^{yy}(\mathbf{x}, t_n) + \delta t \mathcal{G}^{yy}(\mathbf{u}^{(n+1)}, \boldsymbol{\tau}(\mathbf{x}, t_n)), \tag{13}$$

$$\overline{\tau^{xy}}(\mathbf{x}, t_{n+1}) = \tau^{xy}(\mathbf{x}, t_n) + \delta t \mathcal{G}^{xy}(\mathbf{u}^{(n+1)}, \boldsymbol{\tau}(\mathbf{x}, t_n)), \tag{14}$$

2. Compute $\tau^{xx}(\mathbf{x}, t_{n+1}), \tau^{yy}(\mathbf{x}, t_{n+1}), \tau^{xy}(\mathbf{x}, t_{n+1})$ from equations

$$\begin{aligned}
\tau^{xx}(\mathbf{x}, t_{n+1}) = \tau^{xx}(\mathbf{x}, t_n) + \frac{\delta t}{2} \Big[& \mathcal{G}^{xx}(\mathbf{u}^{(n+1)}, \boldsymbol{\tau}(\mathbf{x}, t_n)) \\
& + \mathcal{G}^{xx}(\mathbf{u}^{(n+1)}, \overline{\boldsymbol{\tau}}(\mathbf{x}, t_{n+1})) \Big],
\end{aligned} \tag{15}$$

$$\begin{aligned}
\tau^{yy}(\mathbf{x}, t_{n+1}) = \tau^{yy}(\mathbf{x}, t_n) + \frac{\delta t}{2} \Big[& \mathcal{G}^{yy}(\mathbf{u}^{(n+1)}, \boldsymbol{\tau}(\mathbf{x}, t_n)) \\
& + \mathcal{G}^{yy}(\mathbf{u}^{(n+1)}, \overline{\boldsymbol{\tau}}(\mathbf{x}, t_{n+1})) \Big],
\end{aligned} \tag{16}$$

$$\begin{aligned}
\tau^{xy}(\mathbf{x}, t_{n+1}) = \tau^{xy}(\mathbf{x}, t_n) + \frac{\delta t}{2} \Big[& \mathcal{G}^{xy}(\mathbf{u}^{(n+1)}, \boldsymbol{\tau}(\mathbf{x}, t_n)) \\
& + \mathcal{G}^{xy}(\mathbf{u}^{(n+1)}, \overline{\boldsymbol{\tau}}(\mathbf{x}, t_{n+1})) \Big].
\end{aligned} \tag{17}$$

The expressions of $\mathcal{G}^{xx}(\mathbf{u}, \boldsymbol{\tau}), \mathcal{G}^{yy}(\mathbf{u}, \boldsymbol{\tau}), \mathcal{G}^{xy}(\mathbf{u}, \boldsymbol{\tau})$ are given in equations (7a) - (7c). The tensor $\boldsymbol{\tau}(\mathbf{x}, t_{n+1})$ is computed on cell centres and therefore, $\mathcal{G}^{xx}(\mathbf{u}^{(n+1)}, \boldsymbol{\tau}(\mathbf{x}, t_n)), \mathcal{G}^{yy}(\mathbf{u}^{(n+1)}, \boldsymbol{\tau}(\mathbf{x}, t_n)),$

$\mathcal{G}^{xy}(\mathbf{u}^{(n+1)}, \boldsymbol{\tau}(\mathbf{x}, t_n))$, are approximated by the following difference equations

$$\mathcal{G}_{i,j}^{xx} = -\mathbf{conv}(u^{n+1}\tau^{xx})\big|_{i,j} - \mathbf{conv}(v^{n+1}\tau^{xx})\big|_{i,j} + 2\left(\frac{u_{i+\frac{1}{2},j}^{n+1} - u_{i-\frac{1}{2},j}^{n+1}}{\delta x}\tau_{i,j}^{xx}\right)$$
$$+ 2\left(\frac{u_{i,j+\frac{1}{2}}^{n+1} - u_{i,j-\frac{1}{2}}^{n+1}}{\delta y}\tau_{i,j}^{xy}\right) - \frac{1}{Wi}\left\{\tau_{i,j}^{xx} + \frac{\alpha ReWi}{1-\beta}[(\tau_{i,j}^{xx})^2 + (\tau_{i,j}^{xy})^2]\right\} \qquad (18)$$
$$+ 2\frac{(1-\beta)}{ReWi}\left(\frac{u_{i+\frac{1}{2},j}^{n+1} - u_{i-\frac{1}{2},j}^{n+1}}{\delta x}\right),$$

$$\mathcal{G}_{i,j}^{xy} = -\mathbf{conv}(u^{n+1}\tau^{xy})\big|_{i,j} - \mathbf{conv}(v^{n+1}\tau^{xy})\big|_{i,j} + \left(\frac{u_{i+\frac{1}{2},j}^{n+1} - u_{i-\frac{1}{2},j}^{n+1}}{\delta x} + \frac{v_{i,j+\frac{1}{2}}^{n+1} - v_{i,j-\frac{1}{2}}^{n+1}}{\delta y}\right)\tau_{i,j}^{xy}$$
$$+ \frac{u_{i,j+\frac{1}{2}}^{n+1} - u_{i,j-\frac{1}{2}}^{n+1}}{\delta y}\tau_{i,j}^{yy} + \frac{v_{i+\frac{1}{2},j}^{n+1} - v_{i-\frac{1}{2},j}^{n+1}}{\delta x}\tau_{i,j}^{xx} - \frac{1}{Wi}\left[\tau_{i,j}^{xy} + \frac{\alpha ReWi}{1-\beta}\tau_{i,j}^{xy}(\tau_{i,j}^{xx} + \tau_{i,j}^{yy})\right] \quad (19)$$
$$+ \frac{1-\beta}{ReWi}\left(\frac{u_{i,j+\frac{1}{2}}^{n+1} - u_{i,j-\frac{1}{2}}^{n+1}}{\delta y} + \frac{u_{i+\frac{1}{2},j}^{n+1} - u_{i-\frac{1}{2},j}^{n+1}}{\delta x}\right),$$

$$\mathcal{G}_{i,j}^{yy} = -\mathbf{conv}(u^{n+1}\tau^{yy})\big|_{i,j} - \mathbf{conv}(v^{n+1}\tau^{yy})\big|_{i,j} + 2\left(\frac{v_{i+\frac{1}{2},j}^{n+1} - v_{i-\frac{1}{2},j}^{n+1}}{\delta x}\tau_{i,j}^{xy}\right)$$
$$+ 2\left(\frac{v_{i,j+\frac{1}{2}}^{n+1} - v_{i,j-\frac{1}{2}}^{n+1}}{\delta y}\tau_{i,j}^{yy}\right) - \frac{1}{Wi}\left\{\tau_{i,j}^{yy} + \frac{\alpha ReWi}{1-\beta}[(\tau_{i,j}^{xy})^2 + (\tau_{i,j}^{yy})^2]\right\} \qquad (20)$$
$$+ 2\frac{(1-\beta)}{ReWi}\left(\frac{v_{i,j+\frac{1}{2}}^{n+1} - v_{i,j-\frac{1}{2}}^{n+1}}{\delta y}\right),$$

where

$$u_{i,j+\frac{1}{2}}^{n+1} = \frac{u_{i-\frac{1}{2},j}^{n+1} + u_{i-\frac{1}{2},j+1}^{n+1} + u_{i+\frac{1}{2},j}^{n+1} + u_{i+\frac{1}{2},j+1}^{n+1}}{4}, \quad u_{i,j-\frac{1}{2}}^{n+1} = \frac{u_{i-\frac{1}{2},j}^{n+1} + u_{i-\frac{1}{2},j-1}^{n+1} + u_{i+\frac{1}{2},j}^{n+1} + u_{i+\frac{1}{2},j-1}^{n+1}}{4},$$
$$v_{i+\frac{1}{2},j}^{n+1} = \frac{v_{i,j-\frac{1}{2}}^{n+1} + v_{i+1,j-\frac{1}{2}}^{n+1} + v_{i,j+\frac{1}{2}}^{n+1} + v_{i+1,j+\frac{1}{2}}^{n+1}}{4}, \quad v_{i-\frac{1}{2},j}^{n+1} = \frac{v_{i,j-\frac{1}{2}}^{n+1} + v_{i-1,j-\frac{1}{2}}^{n+1} + v_{i,j+\frac{1}{2}}^{n+1} + v_{i-1,j+\frac{1}{2}}^{n+1}}{4}.$$

The convective terms $\mathbf{conv}(\mathbf{u}^{n+1}\boldsymbol{\tau})\big|_{i,j}$ are calculated by the CUBISTA method [3]. This is a high order scheme that requires remote-upstream, upstream and downstream values of the variable that is being approximated and therefore, for points near rigid boundaries, the values of the components of the extra-stress tensor in boundary cells are required. These values can be estimated by making linear interpolation using internal values of the variables. For instance, with reference to the boundary cell shown in figure 4, the calculation of the components of $\boldsymbol{\tau}$ is effected by

$$\tau_{i,j}^{xx} = 2 * \tau_{i-1,j}^{xx} - \tau_{i-2,j}^{xx} \qquad (21a)$$

$$\tau_{i,j}^{xy} = 2 * \tau_{i-1,j}^{xy} - \tau_{i-2,j}^{xy} \qquad (21b)$$

$$\tau_{i,j}^{yy} = 2 * \tau_{i-1,j}^{yy} - \tau_{i-2,j}^{yy} \qquad (21c)$$

9

For boundary cells having two-adjacent faces contiguous with internal cells then we apply linear interpolation in each direction and the estimated value set in the boundary cell is the average of the values obtained in the each direction.
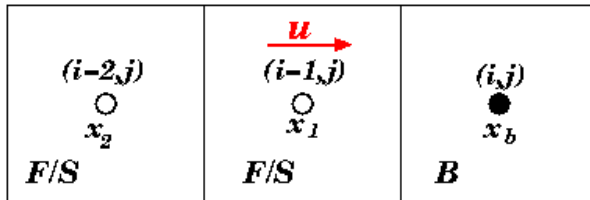

Figure 4: Calculation of the extra-stress components in boundary cells having the left-face adjacent to internal (F/S) cells.

4   Verification results

The resulting finite difference equations from the approximation of the governing equations for the flow of Giesekus fluids were implemented in a computer code that simulates flows governed by the Giesekus model. To verify the correctness of the code and the methodology employed, the flow in a channel was simulated. At the channel entrance (see figure 5), a Newtonian flow profile given by

$$u(y) = -4\frac{U}{L^2}\Big(y - \frac{L}{2}\Big)^2 + U \quad \text{e} \quad v(y) = 0, \tag{22}$$

was especified. The data employed are displayed in Table 1 which gave $Re = 1$ and $Wi = 1$. To
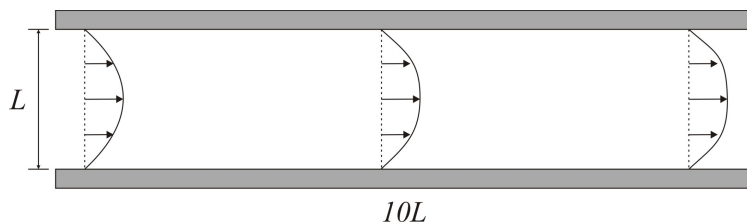

Figure 5: Domínio computacional de um canal bidimensional.

verify the convergence of the numerical method, this problem was simulated in 5 meshes defined in Table 2. The simulations started at $t = 0$s and finished at time $t = 100$s where it is expected that steady state has been stablished. Indeed, figure 6 displays the contour lines of u and v at time $t = 100$. The results shown indicate that near the channel entrance there is a small variation of the velocity but from the middle of the channel towards to the end, the isolines of the velocity u are parallel and $v = 0$, what show that steady state has been reached. To demonstrate the convergence of the numerial

10

method, the data used in these simulations were employed to calculate the analytic solutions (see details in Appendix A) which delivered $p_x = \partial p/\partial x = -6.116$. Figure 7 displays the convergence of the values of p_x to the analytic value, with mesh refinement. The numerical value of p_x was calculated by $p_x \approx \left(\sum_{j=1}^{J_l} \frac{p_{i_{out},j} - p_{i_{out-1},j}}{\delta x} \right)/J_l$, where i_{out} denotes the i-index of the column of cells before the channel exit and J_l represents the number of cells in the y-direction of mesh M_l where l stands for 1, 2, $\cdots$, or 5.

Figure 8 displays the numerical solutions obained on the meshes simulated against the respective analytic solution. It can be seen that the agreement between numerical and analytic solutions is good and that the numerical solutions converge to the analytic solutions as the mesh is refined. The theoretical velocity $u(y)$ was obtained by integrating $\partial u/\partial y$ over the interval [0, 1] and it is shown in figure 9 together with the numerical solutions where a good concordance between the computed velocity $u(y)$ is achieved.

To quantitatively show the convergence of the numerical method, the relative errors were calculated by the formula

$$E_{M_l} = \sqrt{\frac{\sum_{j=1}^{j=J_l}(sol_{exata} - sol_{M_l})^2}{\sum_{j=1}^{j=J_l}(sol_{exata})^2}}. \tag{23}$$

Table 3 displays the errors obtained in the five meshes simulated while figure 10 shows the diminishing of the errors with mesh spacing which shows the convergence of the numerical method.

These results verify the code implementation of the Giesekus model on channel flows.

L (m)	U (m/s)	η_0 (Pa.s)	ρ (kg/m^3)	α
0.01	0.1	1	1000	0.1

Table 1: Data employed in the simulation of channel flow.

Meshes	**M1**	**M2**	**M3**	**M4**	**M5**
Size	10×100 ($\delta x = L/10$)	20×200 ($\delta x = L/20$)	30×300 $\delta x = L/30$	40×400 $\delta x = L/40$	50×500 $\delta x = L/50$

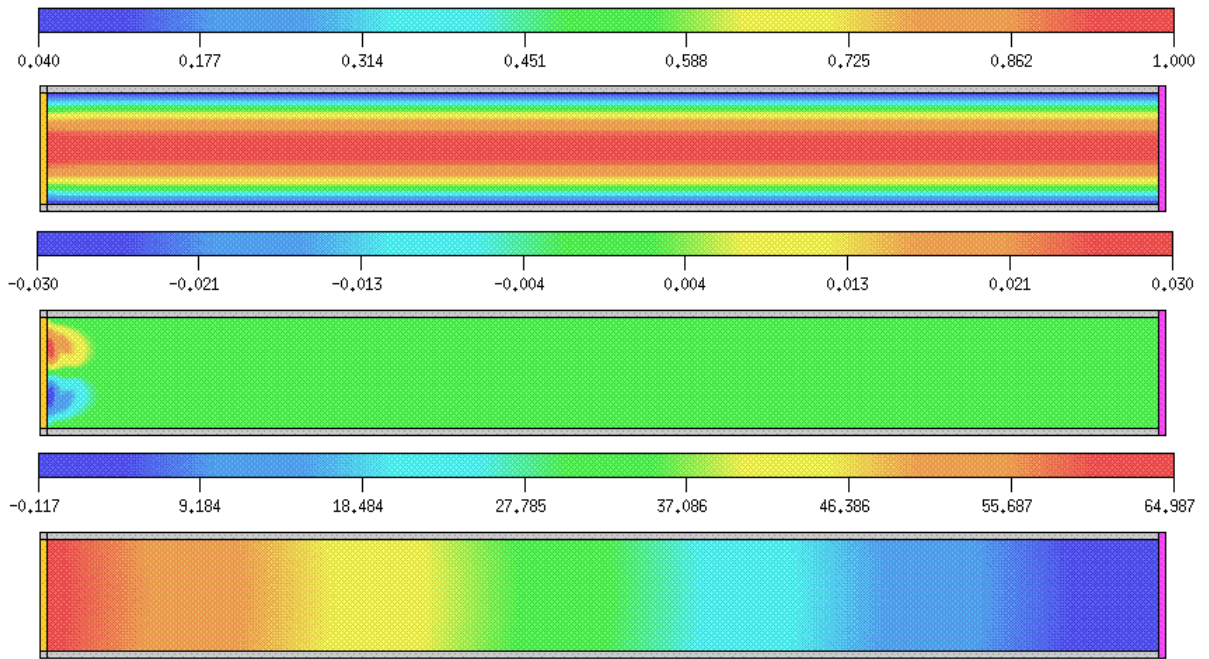Table 2: Definition of the meshes employed to simulate channel flow.

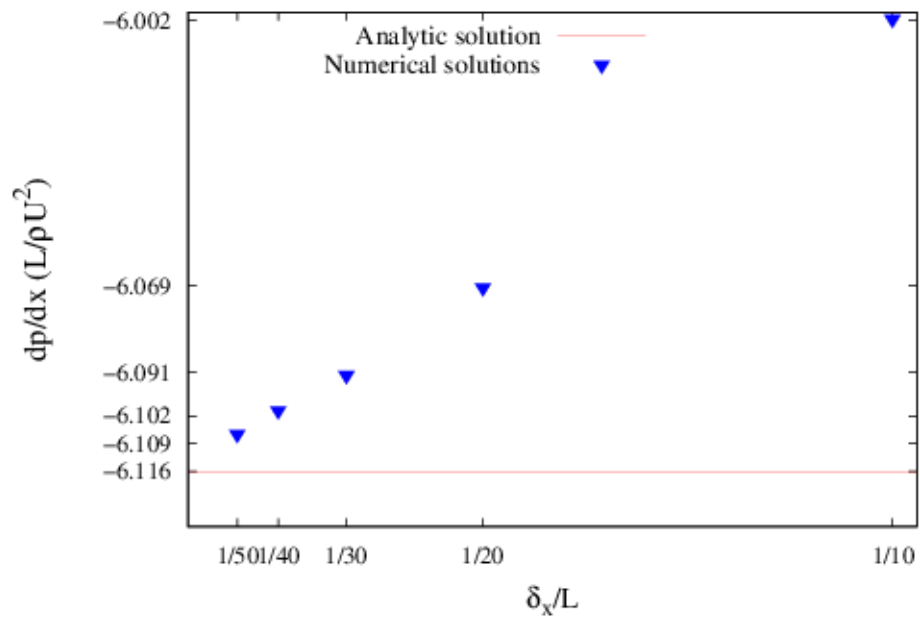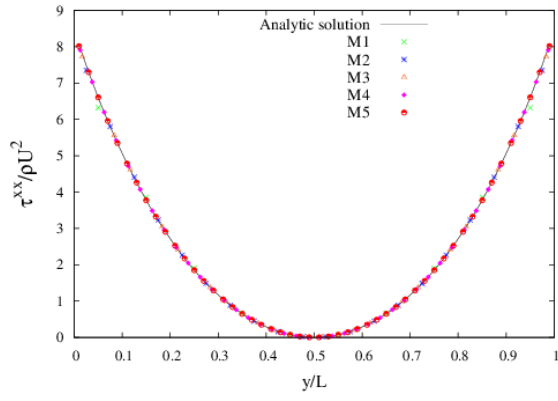Figure 6: Contour lines obtained at $t = 100$. (a) Velocity u; (b) Velocity v; (c) Pressure p.
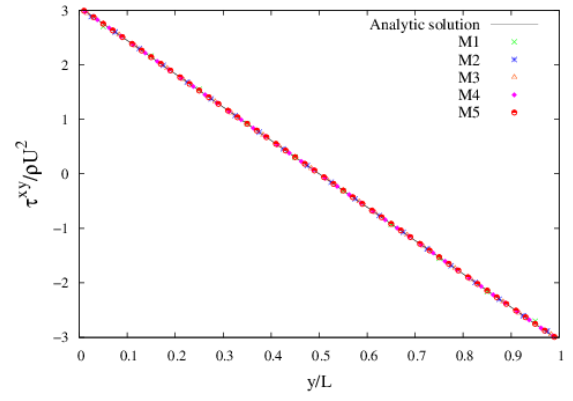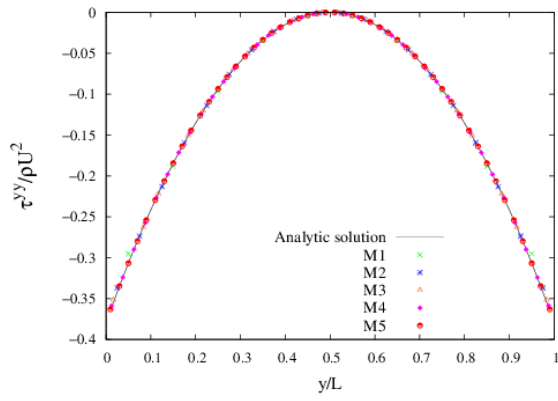

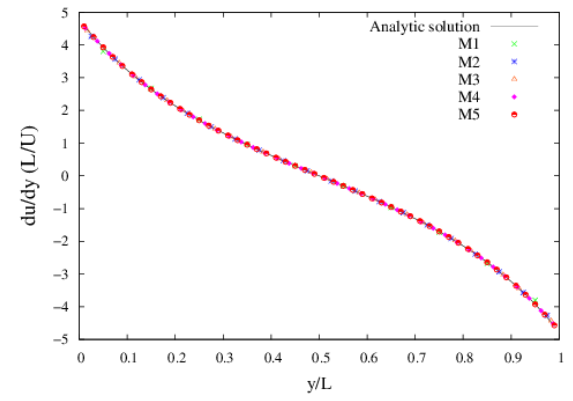Figure 7: Convergence of the numerical values dp/dx to its analytic value with mesh refinement.

Figure 8: Comparison between the numerical and analytic solutions on meshes **M**1, **M**2, **M**3, **M**4 and **M**5. a) τ^{xx}, b) τ^{xy}, c) τ^{yy}, d) du/dy.
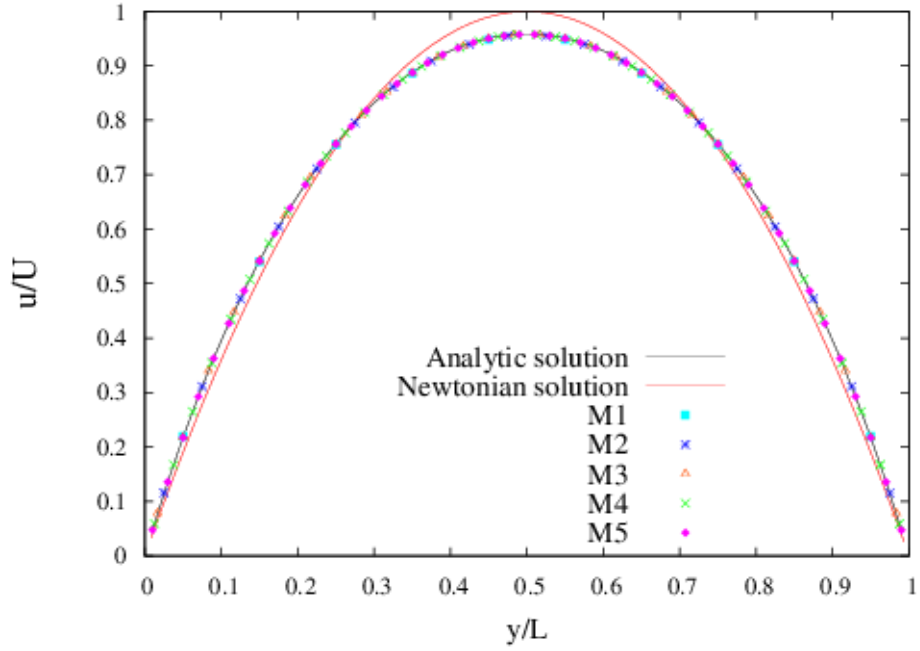
Figure 9: Comparison between the analytic solution $u(y)$ and the velocity u on meshes $\mathbf{M}1$, $\mathbf{M}2$, $\mathbf{M}3$, $\mathbf{M}4$ and $\mathbf{M}5$.

Relative Errors	Meshes				
	M1	**M2**	**M3**	**M4**	**M5**
$E(\tau^{xx})$	$3.690\mathrm{x}10^{-2}$	$1.188\mathrm{x}10^{-2}$	$5.408\mathrm{x}10^{-3}$	$2.982\mathrm{x}10^{-3}$	$1.850\mathrm{x}10^{-3}$
$E(\tau^{xy})$	$1.516\mathrm{x}10^{-2}$	$4.131\mathrm{x}10^{-3}$	$1.825\mathrm{x}10^{-3}$	$1.012\mathrm{x}10^{-3}$	$6.400\mathrm{x}10^{-4}$
$E(\tau^{yy})$	$3.265\mathrm{x}10^{-1}$	$1.009\mathrm{x}10^{-2}$	$4.533\mathrm{x}10^{-3}$	$2.488\mathrm{x}10^{-3}$	$1.543\mathrm{x}10^{-3}$
$E(du/dy)$	$2.585\mathrm{x}10^{-2}$	$8.354\mathrm{x}10^{-3}$	$3.827\mathrm{x}10^{-3}$	$2.120\mathrm{x}10^{-3}$	$1.320\mathrm{x}10^{-3}$

Table 3: Relative errors obtained on meshes $\mathbf{M}1$, $\mathbf{M}2$, $\mathbf{M}3$, $\mathbf{M}4$ and $\mathbf{M}5$, for τ^{xx}, τ^{xy}, τ^{yy} and du/dy.
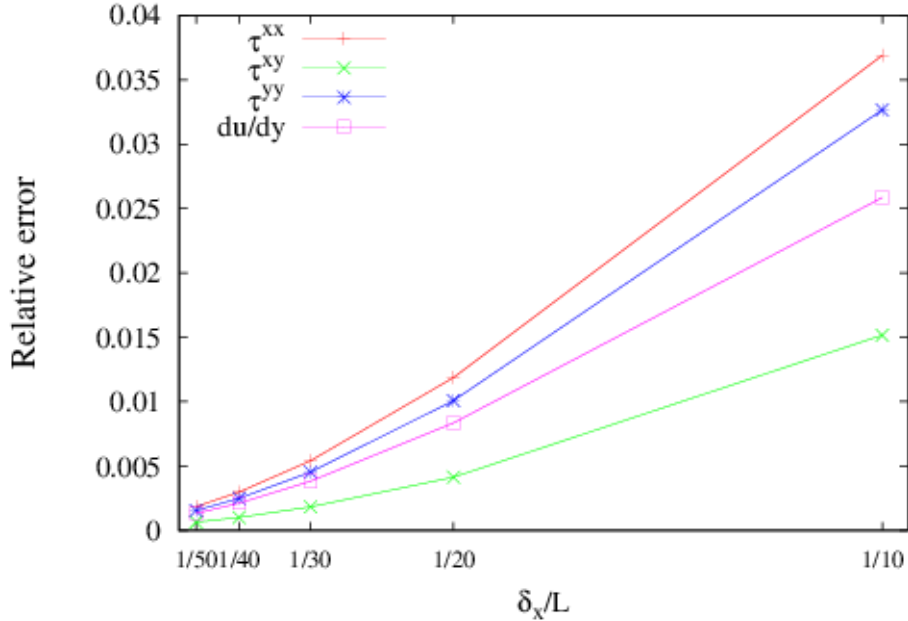
Figure 10: Decaying of errors with mesh spacing.

5   Flow through a planar contraction 4:1

In this section, the results obtained in the simulation of the flow through a planar contraction 4:1 are presented. In this problem, the fluid enters the domain through an entrance channel of width H which at a distance L_2 is contracted into another channel of width $h = H/4$ (see figure 11). The fluid velocity at the entrance channel is given by given by

$$u(y) = -4\frac{U_E}{H^2}\Big(y - \frac{H}{2}\Big)^2 + U_E \quad \text{and} \quad v(y) = 0,\; y \in [0, \quad H]. \tag{24}$$

This problem is very often employed to test codes developed for solving Non-Newtonian flows [73,82,84]. The main interest in this simulation lies in the fact that viscoelastic fluids present different flow patterns when subject to complex geometries like the 4:1 contraction. An effect that has been studied by many researchers is the appearance of a corner vortice as well as a lip vortice on the contraction walls. The size of these vortices can be a consequence of various factors like the Reynolds and Weissenberg numbers, rheological properties of the fluid, among others. This flow behavior has been studied both numerically as well as experimentally (e.g. [60,88,89]). Most of investigations have employed either the UCM, Oldroyd-B and PTT models or a combination of them. Numerical simulations of contraction flows using the Giesekus model have been made only by a few authors [6,61]. More especifically, Choi et al. reported results about the size of the corner vortex as a function of the viscoelastic Mach number

(MA) and found that for small values of MA, the vortex size decreases and from a critical value of MA the vortex size starts to increase. In the work of Joie et al., the results presented involved high values of the Wiessenberg number and the size of the vortex was not reported. In both cases, the Reynolds number employed was not clear.

Next we present results obtained in the simulation of contraction flows using the Giesekus model. The data used in these simulations were as follows:

- Length of the channels: $L_1 = L_2 = 0.16$cm

- $H = 8$cm, $h = H/4 = 2$cm

- Average velocity at the upstream channel: $U_E = 0.025$ms^{-1}

- Length scale; $L = h/2$

- Viscosity: $\eta_P = 1$Pa.s; $\rho = 1000$ kg/m^3

- Giesekus model: $\alpha = 0.1$ and $\lambda = 0.1s$

- Velocity scale: $U = U_E = 0.025$ms^{-1}

These data resulted in $Re = \rho U L/\eta_0 = 1$ and $Wi = \lambda U/L = 1$ The corner vortex was scaled by $L_{vortex} = \dfrac{X}{L}$ where X is shown in figure 11.

To verify the convergence of the numerical method on this problem, the flow through the contraction was simulated on the meshes: **M1** with (40×160)-cells ($\delta_x = \delta_y = 0.002$), **M2** with (80×320)-cells ($\delta_x = \delta_y = 0.001$) and **M3** with (160×640)-cells ($\delta_x = \delta_y = 0.0005$). The simulations started at $t = 0$ until steady state was achieved.

Indeed, figure 12 shows the isolines at $t = 100$s. It can be seen that the u-velocity admits a steady state profile, the v-component of the velocity is almos zero everywhere and the pressure varies linearly through the exit channel. These results show that indicate that steady state has been achieved.

To verify mesh independence results, figures 13 and 14 display, respectively, $p(x)$, dp/dx and u, v, while figure 15 presents the results obtained for τ^{xx}, τ^{xy}, τ^{yy} and $N_1 = \tau^{xx} - \tau^{yy}$, which are plotted on the symmetry axis.

The results in figures 13, 14 and 15 agree well on the three meshes employed and therefore, demonstrate mesh independence of the numerical method applied to this flow problem.

With the purpose of studying vortex development on the contraction walls, a number of simulations with Reynolds numbers $Re = 0.1$ and $Re = 1$ have been performed. To observe elastic effects on the

16

flow, in these simulations, the Wiessenberg number was varied and the parameter α assumed the values of $0.1, 0.3$. The data employed were the same as before, except that the values of Wi were in the range $[0, 5]$ as it is specified in Table 4 and the mesh employed was **Mesh2**. In total, 36 simulations were effected, 9 simulations for each value of α and Re, respectively. Each simulation was carried out until steady state was observed and the size of the corner vortex was measured.

Figure 16 displays the streamlines obtained with $Re = 0.1$ while figure 17 shows those obtained with $Re = 1$.

With reference to figures 16h ($Wi = 4$) and 16i ($Wi = 5$) , a lip vortice can be noticed which becomes larger in figure 16i due to the increase in Wi. The same effect can be observed in figure 17i for $Wi = 5$ and $Re = 1$. To confirm the appearance of these lip vortices, these flows were simulated on a finer mesh with 160×640-cells and the results obtained also showed the appearance of lip vortices for these values of Wi.

The appearance of lip vortices on contraction flows has been reported by several investigators. For instance, this effect is mentioned by Aboubacar and Webster [54] that considered creeping flow ($Re = 0$) and simulated 4:1 contraction flows using an Oldroyd-B fluid. They showed that if $Wi > 1$, a lip vortex might appear. Also, Alves et al. [2] used a finite volume code and presented results from the simulation of contraction flows of PTT and Oldroyd-B fluids. Their main purpose was to investigate the vortex size, vortex intensity and the Couette correction in contraction flows. They performed simulation in a contraction 4:1 employing a long exit channel and reported that the Oldroyd-B model produced a diminishing vortex size with increasing Wiessenberg numbers and a lip vortex was detected at $Wi = 0.5, 1, 1.5$. For the PTT models studied, using $Re = 0$, the results showed a non-monotonic behaviour of the corner vortex size as a function of the Wiessenberg number and the occurrence of lip vortex was not noticed. More recently, Ferrás et al. [1] used the sPTT model para simular the 4:1 contraction flow with $Re = 0$ and $Re = 0.04$ and obtained results for $0 \le Wi \le 5$. With $Wi = 5$, Ferrás et al. [1] showed that an increase of inertia in the flow produced a growing lip vortice that became attached to the corner vortex, forming a large corner vortex that continued to grow with the Wiessenberg number. This effect has been reported both experimentally and numerically for UCM fluids under creeping flow conditions.
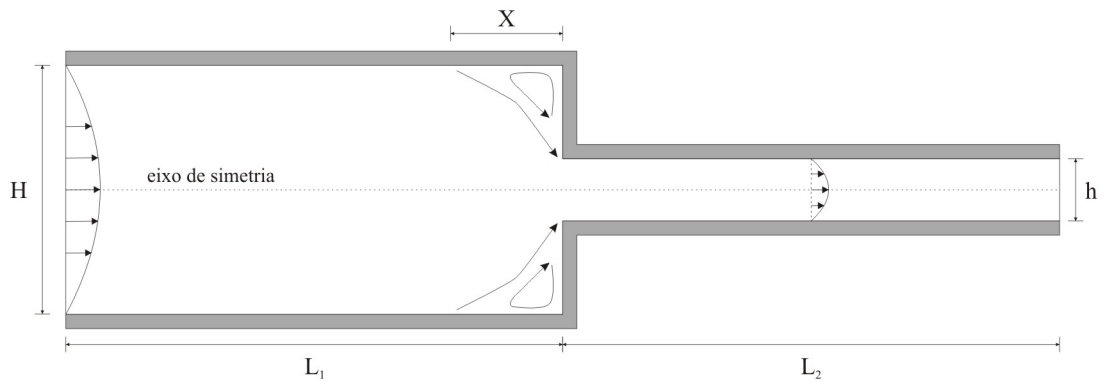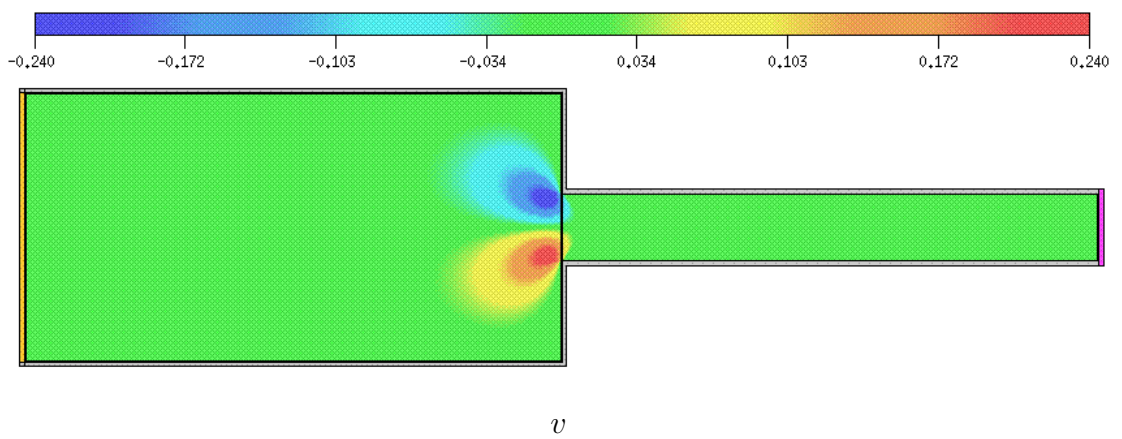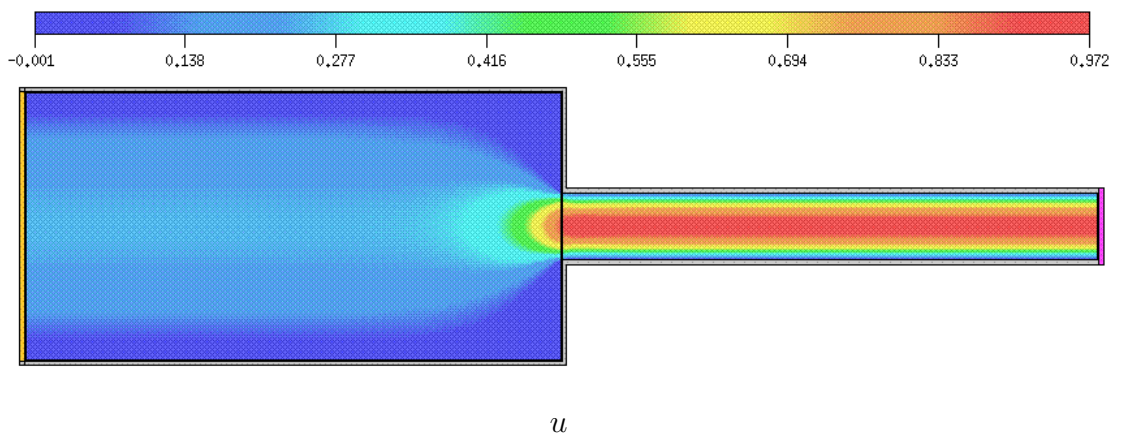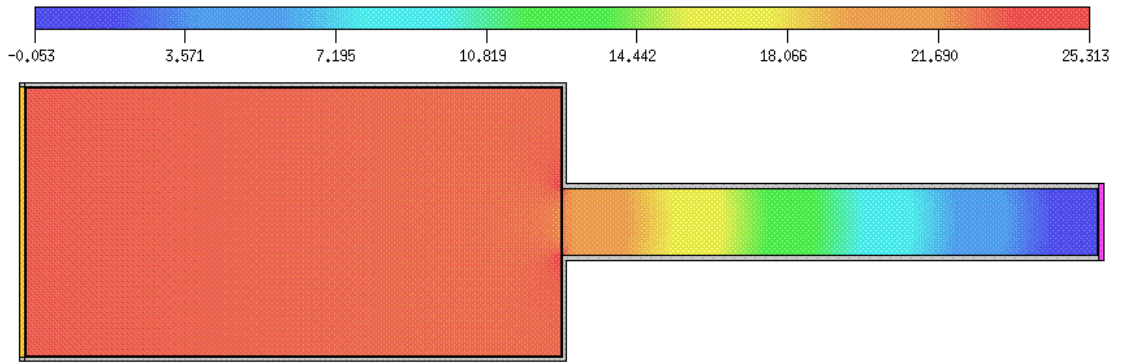
Figure 11: Computational domain for the flow through a 4:1 contraction.

u

v

p

Figure 12: Isolines obtained in the simulation of the flow through a 4:1 contraction at time $t = 100$s. Results shown on mesh **M3**.
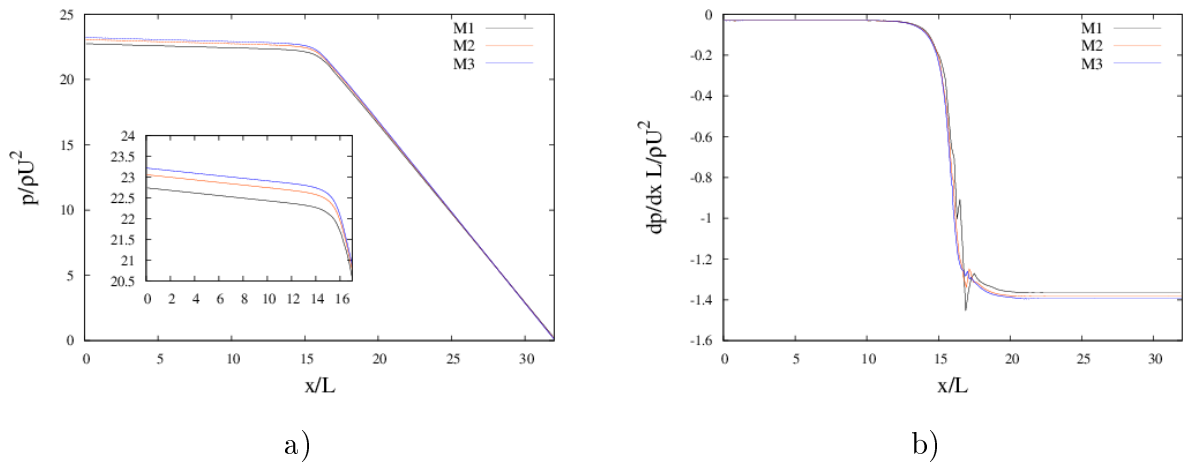

a)

b)

Figure 13: Numerical simulation of the flow through a 4:1 contraction on meshes **M1**, **M2** and **M3**. Results obtained on the symmetry axis. a) Pressure; b) Pressure gradient.
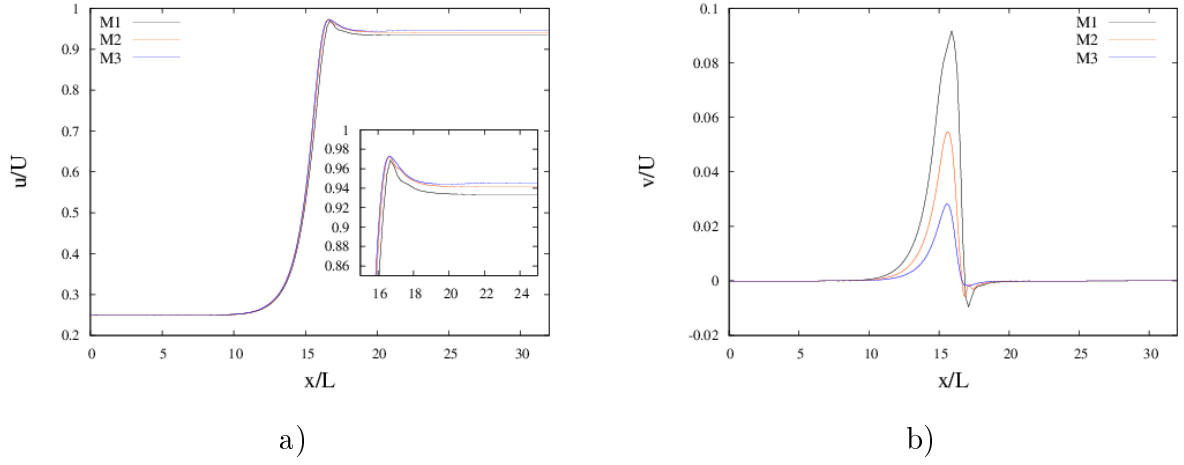
a)

b)

Figure 14: Numerical simulation of the flow through a 4:1 contraction on meshes **M**1, **M**2 and **M**3 on the symmetry axis. a) Velocity $u(x)$; b) Velocity $v(x)$.
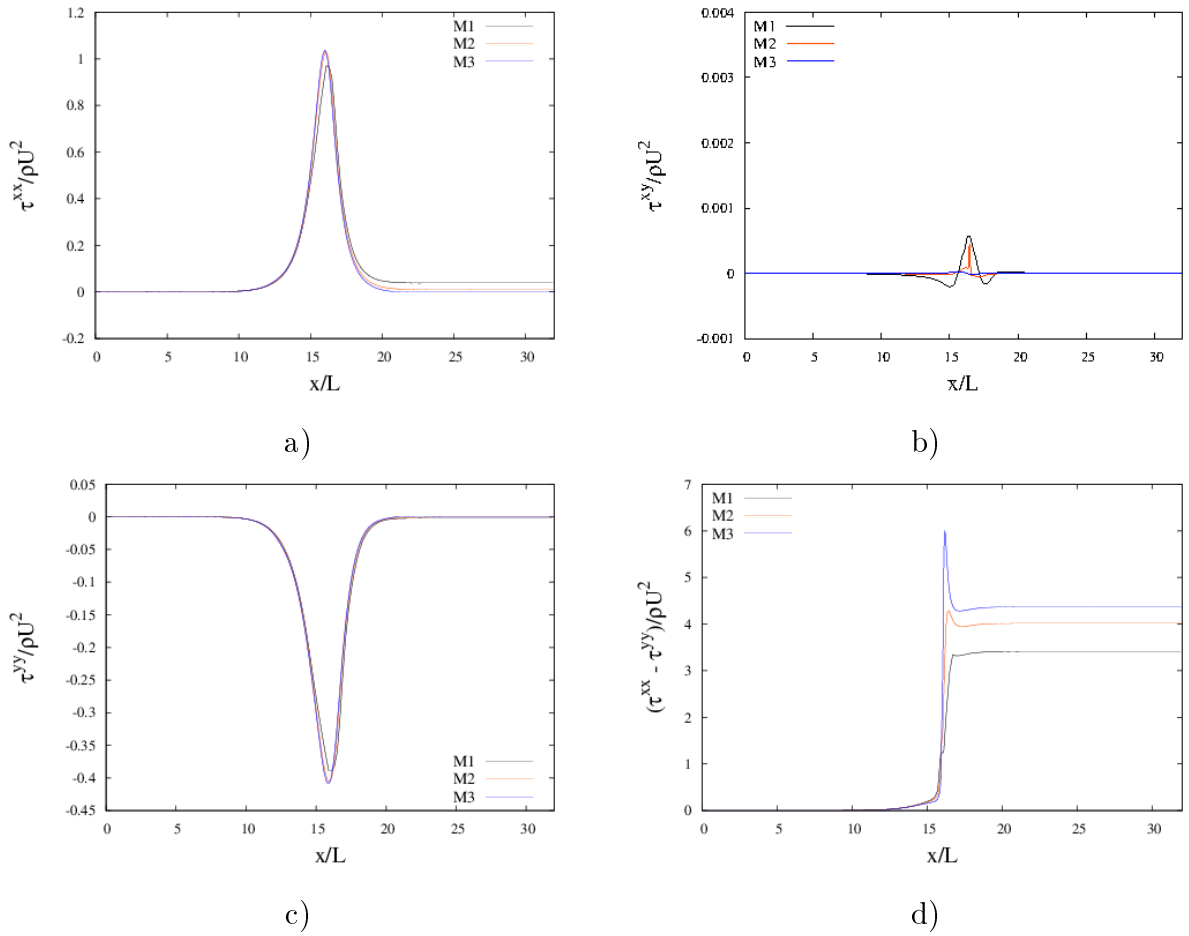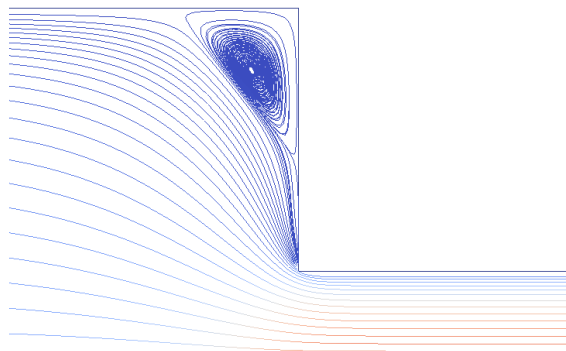

a)

b)

c)

d)

Figure 15: Numerical simulation of the flow through a 4:1 contraction on meshes **M**1, **M**2 and **M**3. Results obtained on the symmetry axis. a) τ^{xx}, b) τ^{xy}, c) τ^{yy} e d) $N_1 = \tau^{xx} - \tau^{yy}$.

λ	0.025	0.05	0.1	0.15	0.2	0.25	0.3	0.4	0.5
Wi	0.25	0.5	1	1.5	2	2.5	3	4	5

Table 4: Values of λ and the associated Wiessenberg numbers.

a)

b)

c)

d)

e)

f)

g)   h)

i)
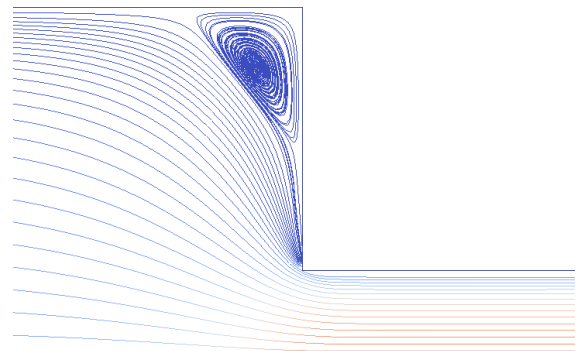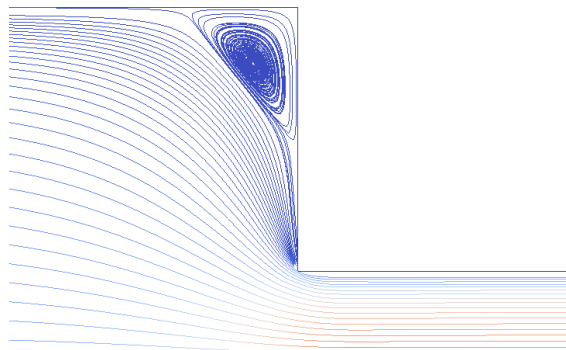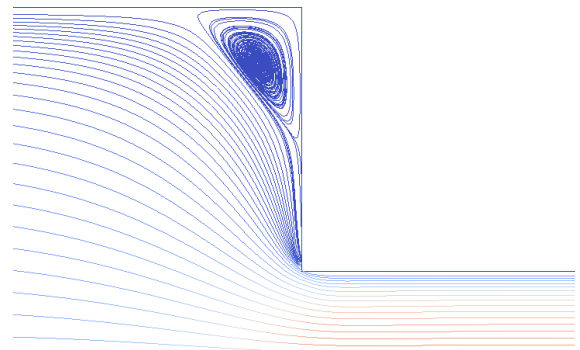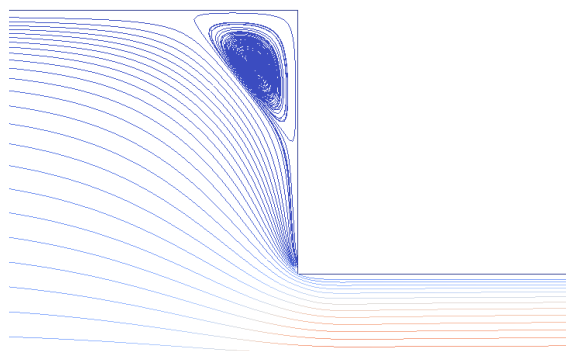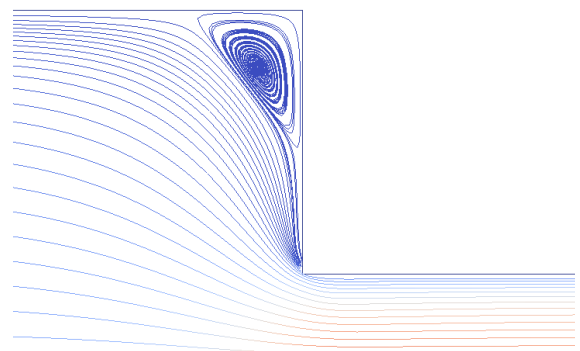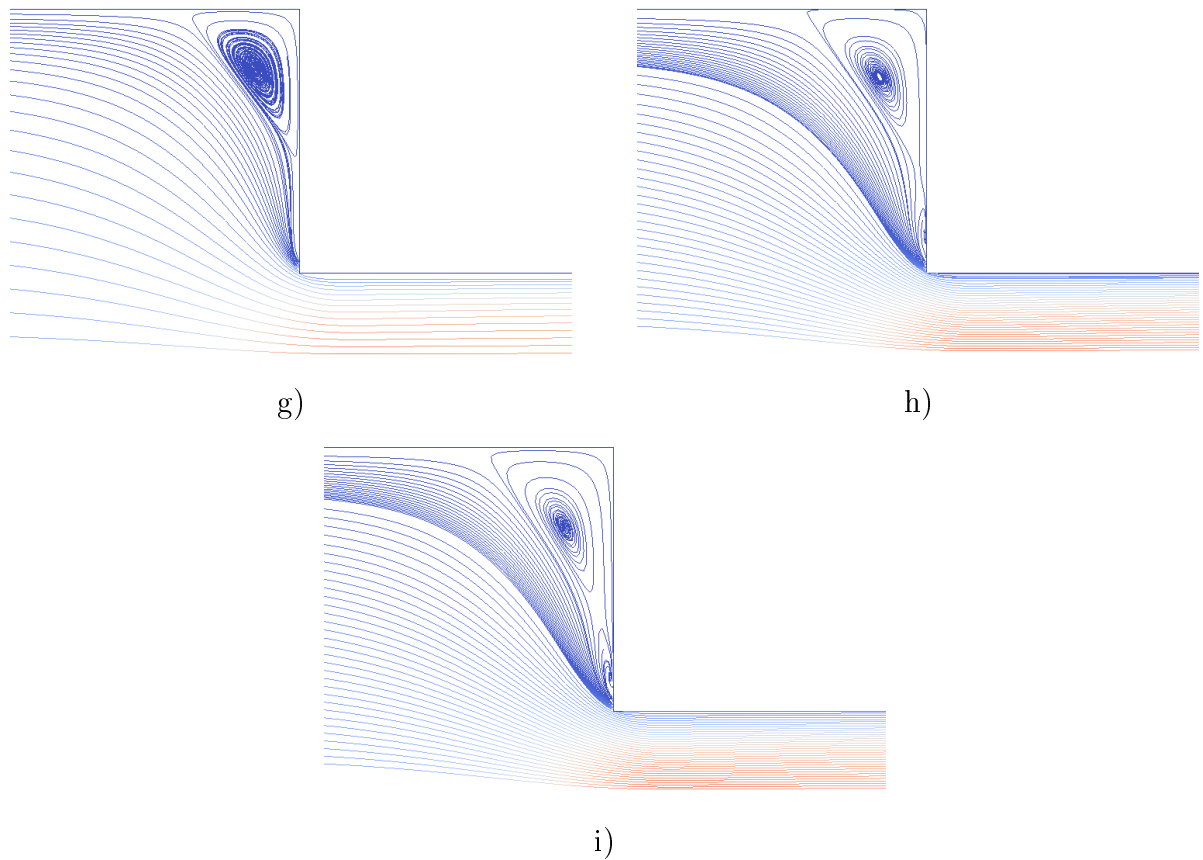
Figure 16: Numerical simulation of the flow through a planar contraction 4:1. Streamlines obtained with $Re = 0.1$ and $\alpha = 0.1$. a) $Wi = 0.25$, b) $Wi = 0.5$, c) $Wi = 1$, d) $Wi = 1.5$, e) $Wi = 2$, f) $Wi = 2.5$, g) $Wi = 3$, h) $Wi = 4$, i) $Wi = 5$.

a)   b)
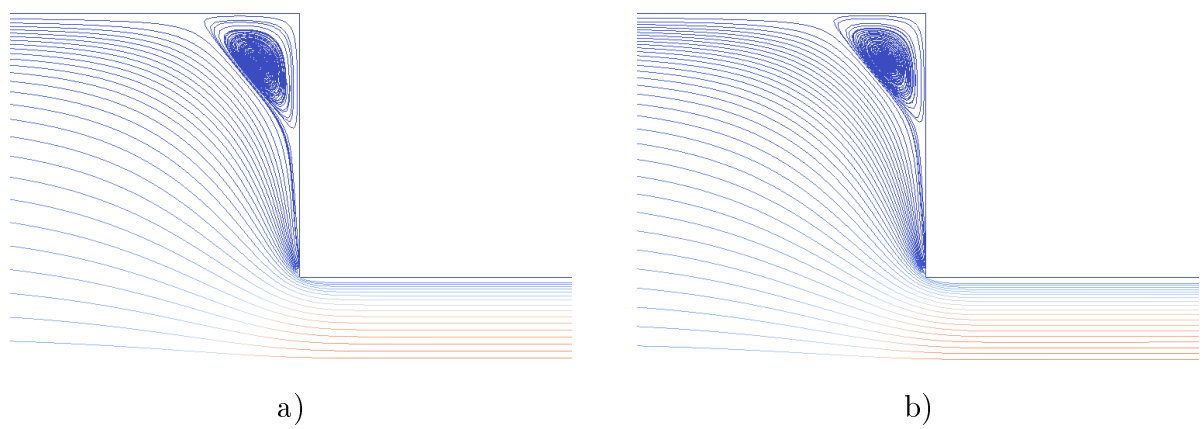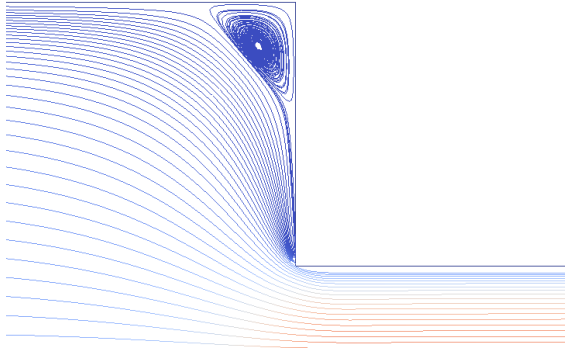
c)
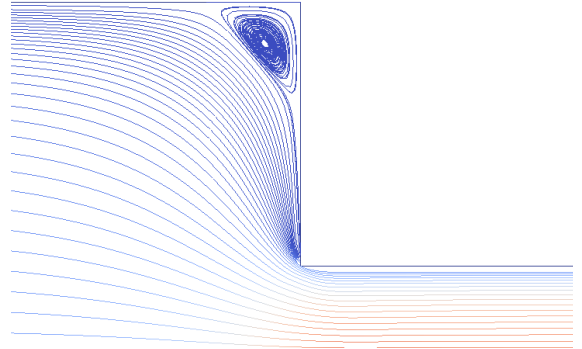
d)
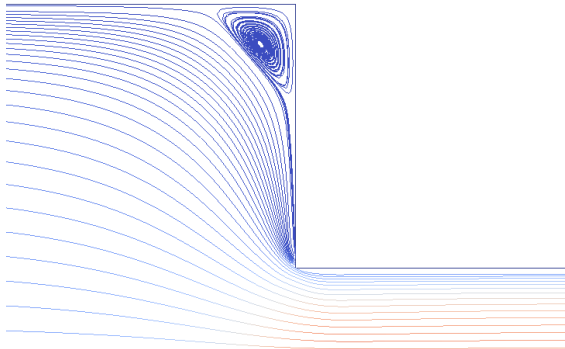
e)
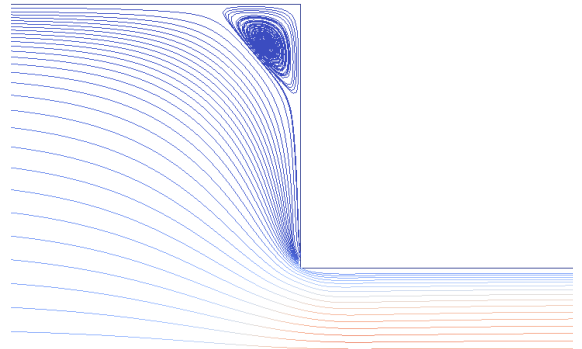
f)
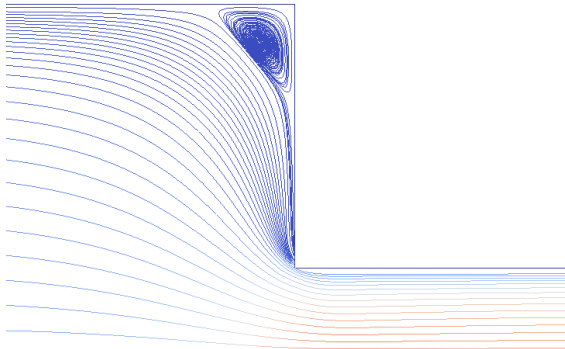
g)
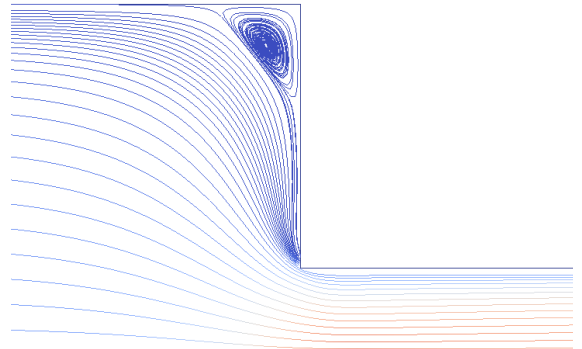
h)
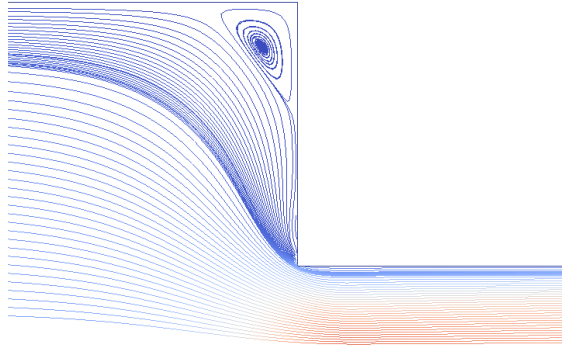
i)

Figure 17: Numerical simulation of the flow through a planar contraction 4:1. Streamlines obtained with $Re = 1$ and $\alpha = 0.1$. a) $Wi = 0.25$, b) $Wi = 0.5$, c) $Wi = 1$, d) $Wi = 1.5$, e) $Wi = 2$, f) $Wi = 2.5$, g) $Wi = 3$, h) $Wi = 4$ e i) $Wi = 5$.

A 5 mostra o tamanho dos vórtices obtidos para cada valor de Wi e a 18 mostra a variação do tamanho do vórtice com o crescimento do número de Weissenberg.

Wi	0.25	0.05	1	1.5	2	2.5	3	4	5
$Re = 0.1$	1.422	1.387	1.339	1.325	1.321	1.333	1.354	1.429	1.535
$Re = 1$	1.230	1.186	1.120	1.076	1.043	1.026	1.018	1.028	1.070

Table 5: Length of the corner vortice as a function of the Weissenberg number for $Re = 0.1, 1$, with $\alpha = 0.1$.
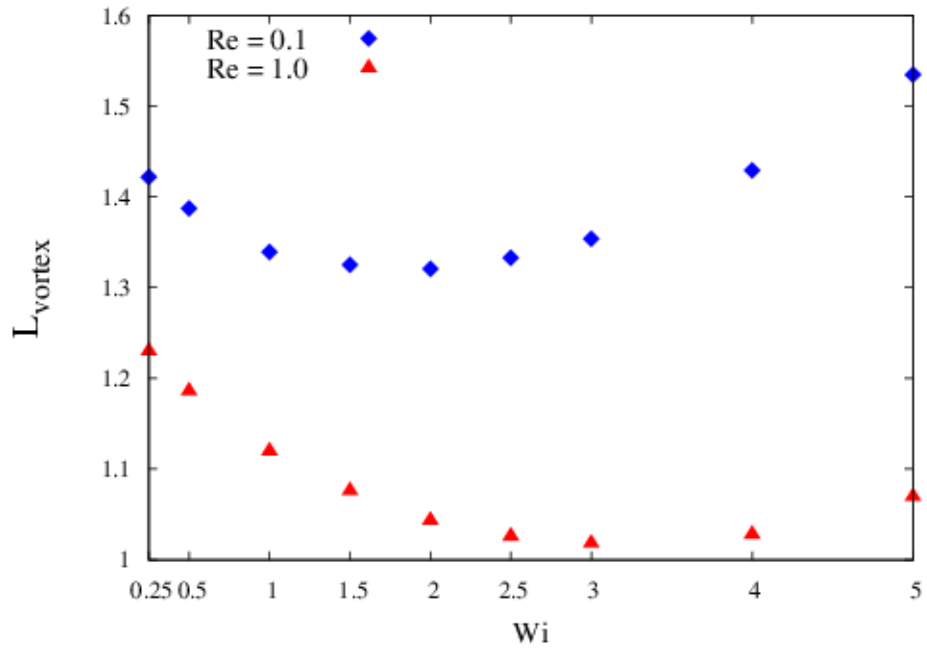
Figure 18: Variation of the length of the corner vortice as a function of the Weissenberg number for $Re = 0.1, 1$, with $\alpha = 0.1$.

6 Simulation of jet buckling of Giesekus fluids

This section contains the results obtained in the simulation of a free surface flow produced by a jet flowing onto a horizontal rigid plate. It is known that, under certain conditions, after the jet flows over the rigid plate, a Newtonian jet can display the phenomenon of jet buckling. This problem has been investigated using several constitutive models such that UCM, Oldroy-B, PTT, XPP, among others and it was shown that elasticity can make the jet to go buckling (see [28,43,44,46,48,49,53,81,83,84]). In particular, [66] and [65] performed a series of experiments showing a Newtonian jet undergoing buckling and obtained conditions based on the Reynolds number (Re)and the height of the inlet jet to the horizontal plate (H) for which jet buckling occurs (see figure 19). Cruckshank [65] showed that a two-dimensional jet should buckle when the following conditions

$$Re < 0.56 \qquad e \qquad H/L_{inj} > 3\pi \tag{25}$$

are satisfied.
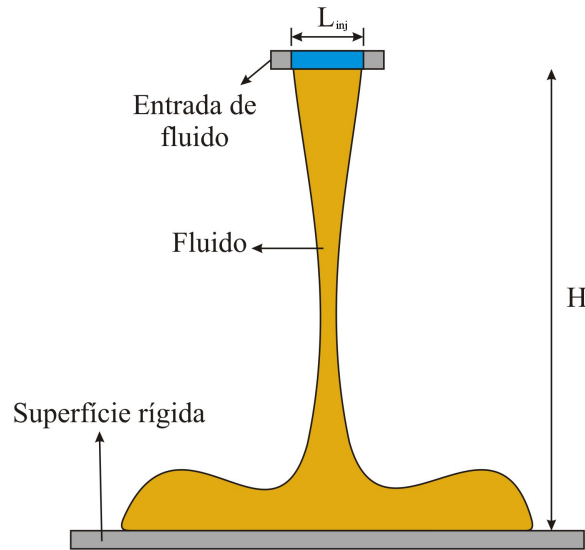
Figure 19: Domínio computacional para a simulação do jet buckling.

To demonstrate that the Giesekus model can simulate this phenomenon, a number of simulations have been performed in which the Wiessenberg number and the Giesekus mobility parameter α were varied in the interval [0, 0.5]. For comparison, the results obtained with a respective Newtonian jet are were also simulated.

The input data employed in these simulations were:

- Domain size: 10cm×12.6cm

- Mesh: $\delta x = \delta y = 0.01$cm ($100 \times 126$ cells)

- Gravitational constant: $g = 9.81 \text{ms}^{-2}$

- Height of the inlet: $H = 12$cm

- Size of the inlet: $L_{inj} = 0.08$cm

- Inlet velocity: $U = 0.2 \text{ms}^{-1}$

- Fluid definition:

  - Fluid viscosity: $\eta = 0.0025 \text{m}^2\text{s}^{-1}$,   Fluid density: $\rho = 1000 \text{kgm}^{-3}$

  - Giesekus model: $\alpha = 0.1,\ 0.3,\ 0.5,\ \beta = 0$ (no solvent), $\lambda = 0.005$s

The scaling parameters U, L, $\nu = \eta/\rho$, λ, lead to: $Re = U\,L/\nu = 0.8$ and $Wi = \lambda\,U/L = 0.1$. Thus, $Re = 0.8 > 0.56$ and $H/L_{inj} = 15 > 3\pi$, so that the Cruickshank conditions (25) are not satisfied and therefore, the simulation with the Newtonian jet is expected to not present the effect of jet buckling. With regard to the jet containing the Giesekus fluid, no conclusion can be drawn as Cruickshank's analysis applies only to Newtonian jets.

Figure 20 displays the fluid flow configuration from these simulations for both the Newtonian and the viscoelastic Giesekus jets at selected times. We can see in figure 20 that at time $t = 0.12$s the results from the simulations are similar; they show the jets being issued from the inlet before reaching the rigid plate below the inlet. Then, at time $t = 0.28$s all the jets have reached the rigid plate and we can observe that the jets started to flow radially and display similar fluid flow configuration. However, at time $t = 0.48$s the jet with $\alpha = 0.1$ already displays the buckling effect while the Newtonian jet flows steadilly in the x-direction; the other two jets ($\alpha = 0.3, 0.5$) start presenting small asymmetries and at times $t = 0.64, 0.80$s the jets with $\alpha = 0.1, 0.3$ exhibit buckling while the jet with $\alpha = 0.5$ starts ondullating and does not present buckling at this time. We believe that these results agree with the Giesekus model that predicts more shear thinning when increasing the value of α. The results showed that $\alpha = 0.5$ provided more mobility, due to the decrease in viscosity, which prevented the buckling phenomenon.

To demonstrate that the buckling effect shown in figure 20 was a consequence of elastic forces, we performed two additional simulations in which the only change in the input data was the value of the Wiessenberg number. The Wiessenberg numbers used in these simulations were $Wi = 1, 2$ so we expect that the effects of elasticity would be more pronounced in these two simulations. Indeed, figures 21 and 22 show that at time $t0.28$s the simulations with the three jets having $Wi = 1, 2$ are

flowing onto the rigid plate and the differences between the results shwon are not too noticeable. Notwithstanding, as time progresses the results at times 0.64 and 0.80 show that all the three jets had undergone the buckling phenomenon. These results certify that the effects of elastic forces, represented by the Wiessenberg number, can influence the flow produced by a jet flowing down to a rigid plate and make the jet to buckle.

Newtonian **$\alpha = 0.1$** **$\alpha = 0.3$** **$\alpha = 0.5$**

t = 0.12s

t = 0.28s

t = 0.48s
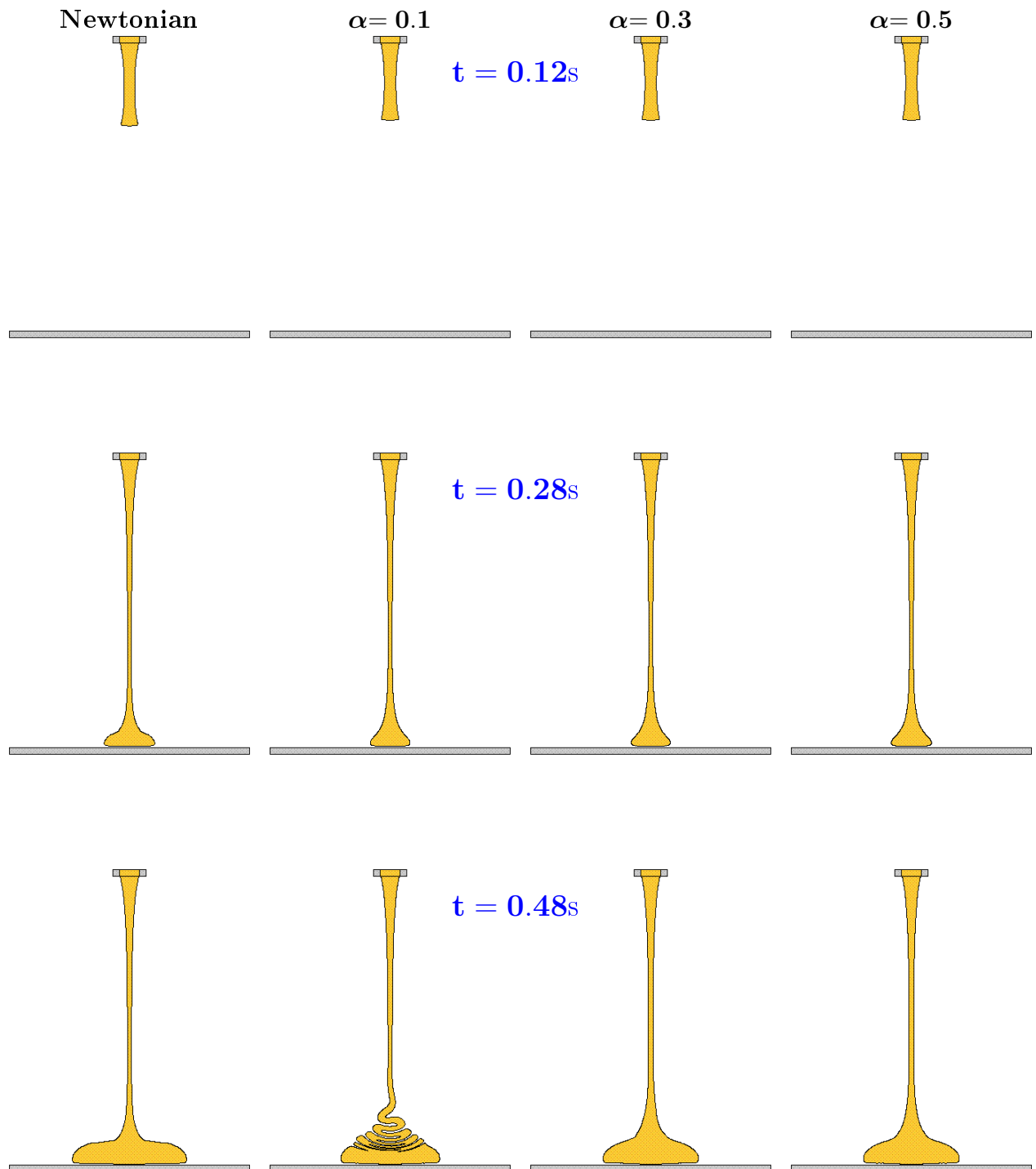
Figure 20: Numerical simulation of a jet flowing down to a rigid plate with $Re = 0.8$ and $Wi = 0.1$, at select times shown. First column: results obtained with a Newtonian jet ($Wi = 0$; Second column: results with $\alpha = 0.1$; Third column: results with $\alpha = 0.3$; Fourth column: results with $\alpha = 0.5$.
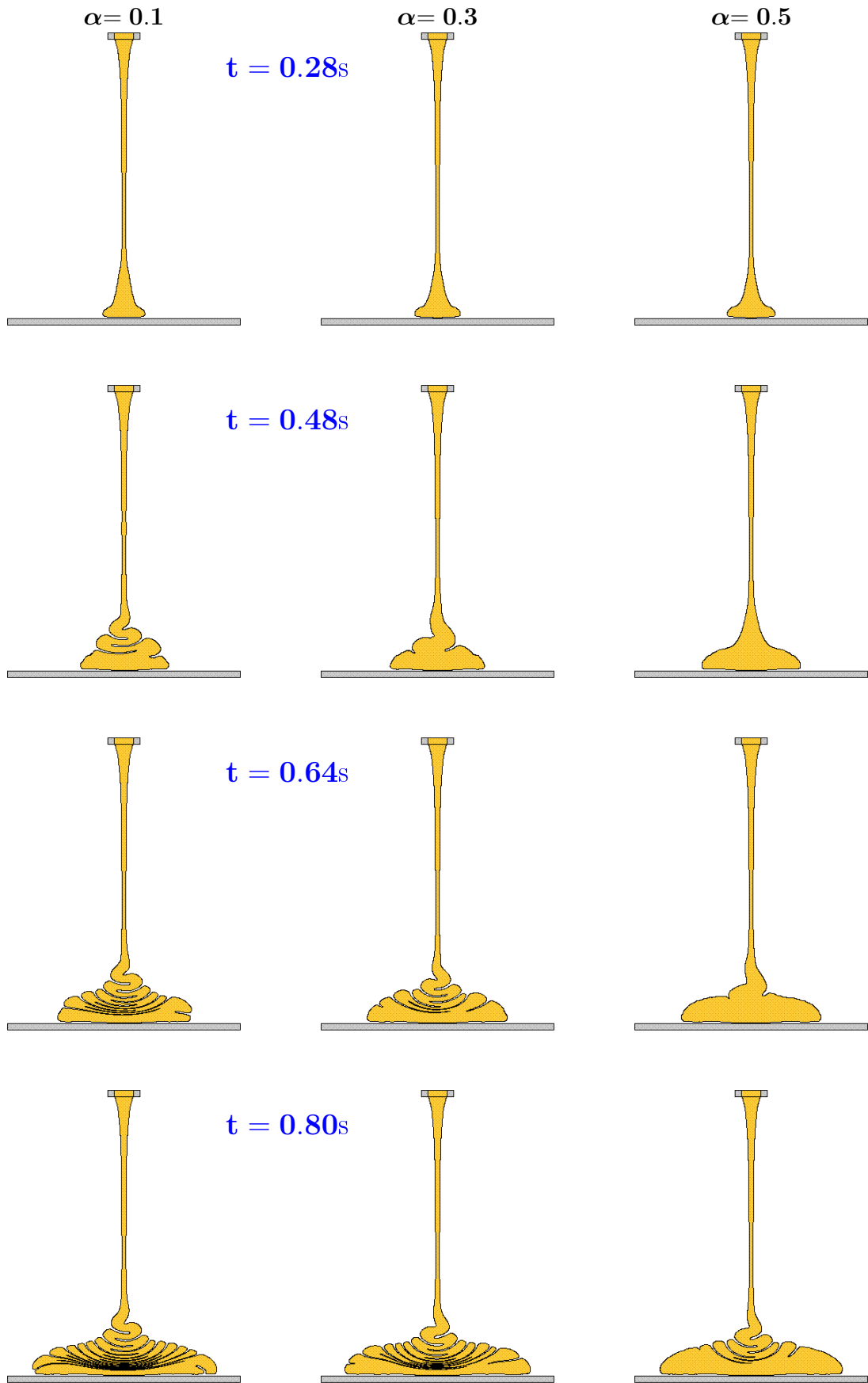
Figure 21: Numerical simulation of a jet flowing down to a rigid plate with $Re = 0.8$ and $Wi = 1$, at select times shown. Results obtained with $\alpha = 0.1, 0.3$ and 0.5.
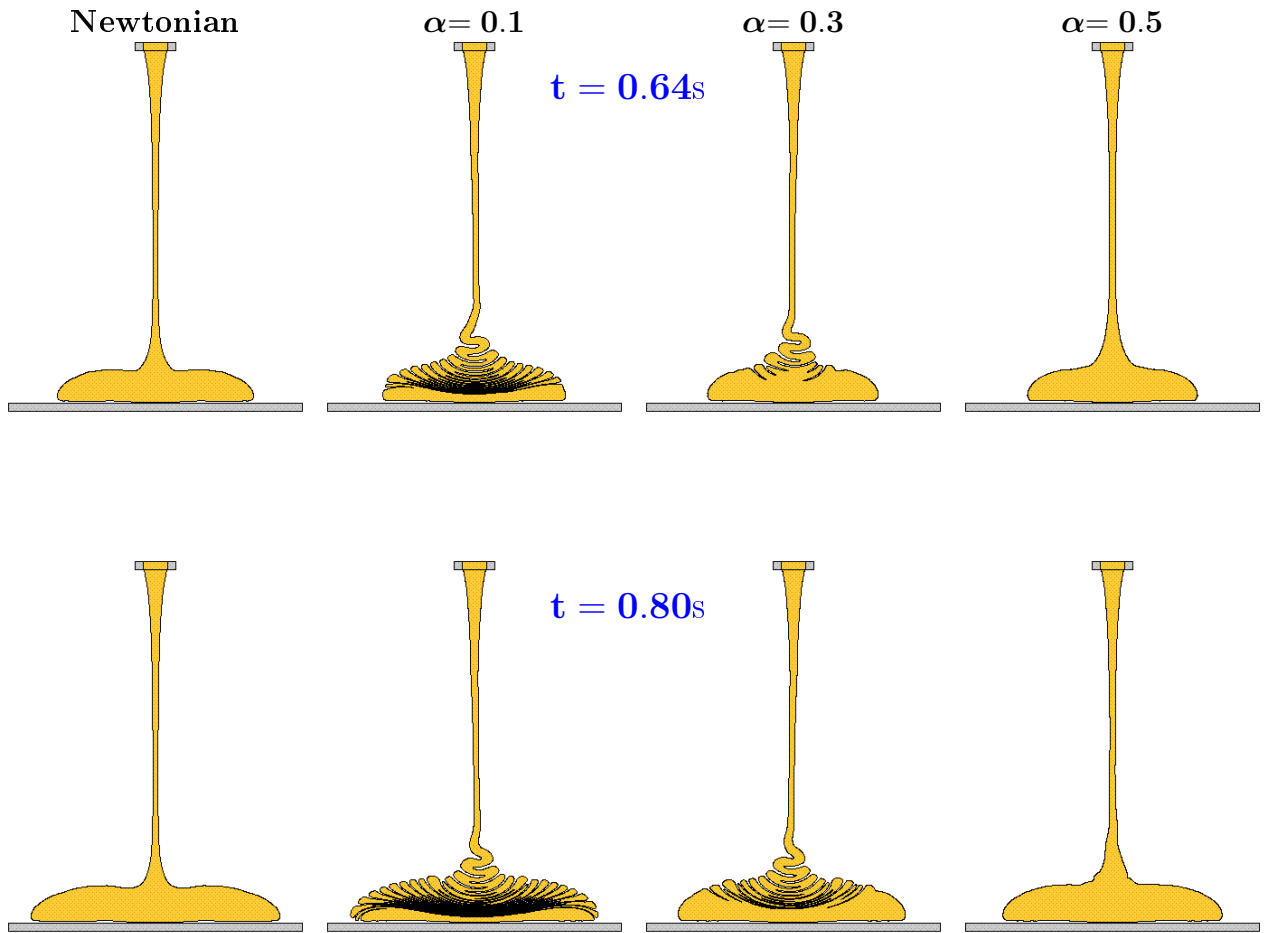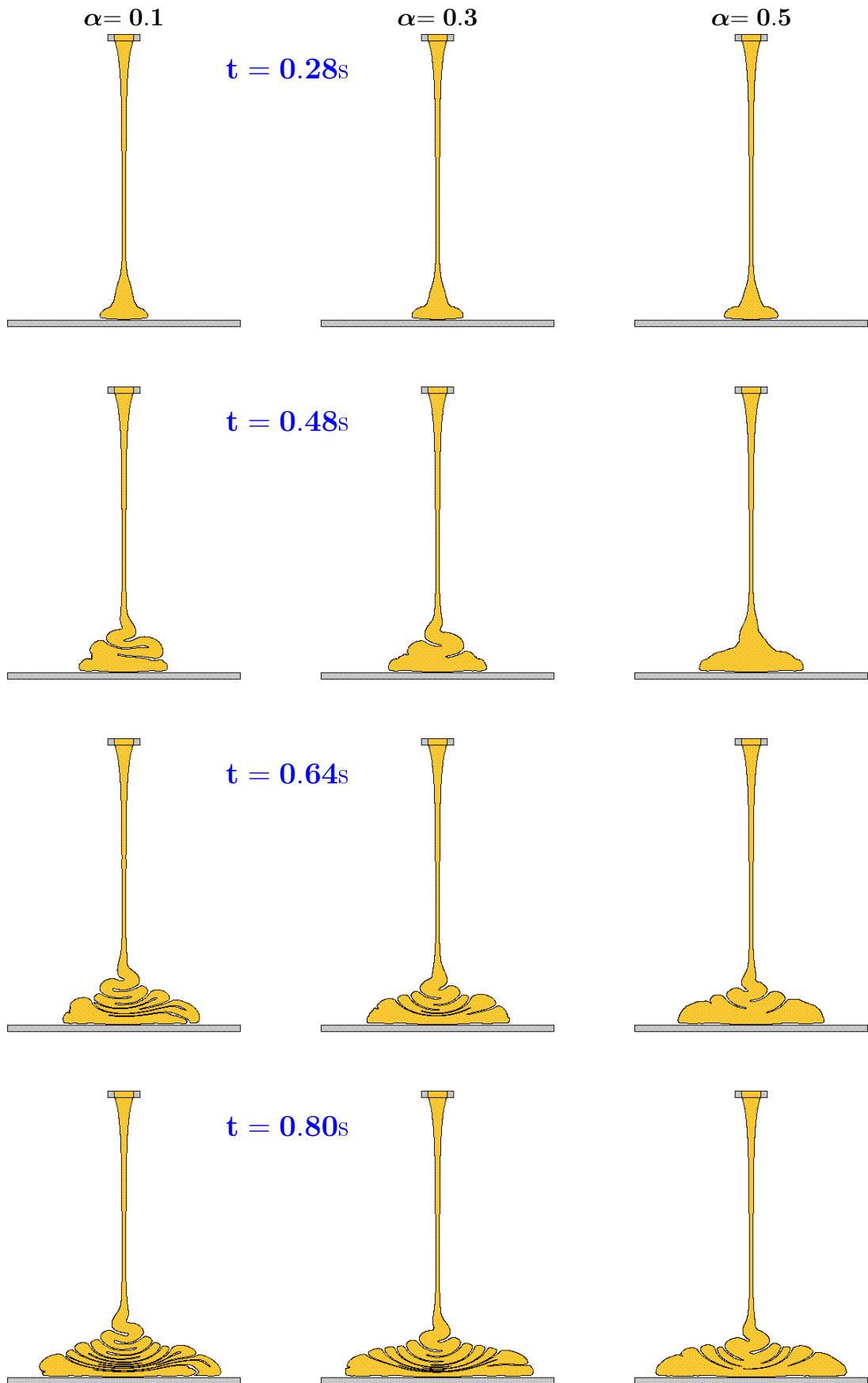
Figure 22: Numerical simulation of a jet flowing down to a rigid plate with $Re = 0.8$ and $Wi = 2$, at select times shown. Results obtained with $\alpha = 0.1, 0.3$ and 0.5.

7 Concluding remarks

This work presented a front tracking technique for solving the Giesekus constitutive equation for incompressible confined and free surface flows. The governing equations were approximated by the finite difference method on a staggered grid. The momentum equations were solved by the implicit Euler method while the solution of the Giesekus equation was obtained by a second order runge-kutta scheme. The developed code was applied to flows governed by the Giesekus model without solvent ($\beta = 0$). The developed technique was quantitatively verified by simulating channel flow and the results were compared with the analytic solution which was derived during the development of this work. The results showed a 2nd order convergence of the numerical technique. The flow through a 4:1 contraction was simulated and a study of the application of the Giesekus model on this problem was performed. First, the flow through a 4:1 contraction was simulated on three meshes which showed mesh independence on this flow problem. Then, flow through a 4:1 abrupt contraction was solved and the effects of varying the Weissenberg number and the mobility parameter α on the flow were investigated. In these simulations, the size of the corner vortex as a function of the Wiessenberg number was monitored which displayed a decrease followed by an increase in size of the corner vortex. Also, a lip vortex was obtained for Wiessenberg numbers $Wi = 4, 5$. These results are novel; the investigations found in the literature only report an increase with Wi for a fixed value of $\alpha = 0.5$

With regard to free surface flows, a jet flowing down onto a rigid plate using various Weissenberg numbers was simulated. results were

8   APPENDIX

ANALYTIC SOLUTION

We consider a 2D-channel having unity width and fully developed flow, where $\mathbf{u} = (u(y), 0)$, $\dfrac{\partial p}{\partial x} = p_x = \text{constant}$, $\tau^{xy}(y), \tau^{yy}(y), \tau^{xx}(y)$, $y \in [0, 1]$. Under these assumptions, the momentum equations (2) reduce to

$$\tau_y^{xy} = p_x, \tag{26}$$

$$\tau_y^{yy} = p_y, \tag{27}$$

and the Giesekus equation (3) can be written as

$$\tau^{yy} + \alpha\, Re\, Wi[(\tau^{yy})^2 + (\tau^{xy})^2] = 0, \tag{28}$$

$$u_y \tau^{yy} - \frac{1}{Wi}\Big\{\tau^{xy} + \alpha\, Re\, Wi[\tau^{xy}(\tau^{xx} + \tau^{yy})]\Big\} + \frac{1}{Re\, Wi}u_y = 0, \tag{29}$$

$$2u_y \tau^{xy} - \frac{1}{Wi}\Big\{\tau^{xx} + \alpha\, Re\, Wi[(\tau^{xy})^2 + (\tau^{xx})^2]\Big\} = 0. \tag{30}$$

where $u_y(y) = \dfrac{\partial u}{\partial y}$. Equations (26)-(30) must be solved for the unknowns $u_y, p_x, \tau^{xy}, \tau^{yy}$ and τ^{xx}. These solutions are found as follows:

By integrating (26) over the interval $[0, y]$ and applying the symmetry condition, the shear stress τ^{xy} is given by

$$\tau^{xy} = \int_0^y p_x ds = p_x(y - \frac{1}{2}), \quad y \in [0, 1] \text{ (the condition } \tau^{xy} = 0 \text{ when } y = 1/2 \text{ was employed) .} \tag{31}$$

Now, using (28), which is a second order algebraic equation in τ^{yy}, we can evaluate τ^{yy} from

$$\tau^{yy} = \frac{-1 + \sqrt{1 - 4\alpha^2\, Re^2\, Wi^2(\tau^{xy})^2}}{2\alpha\, Re\, Wi}, \text{ where we must have } 1 - 4\alpha^2\, Re^2\, Wi^2(\tau^{xy})^2 \geq 0, \text{ for real solutions.} \tag{32}$$

In this equation, the positive sign of the root was chosen so $\tau^{yy} = 0$ in the middle of channel and it must also provide $\tau^{yy} = 0$ if $\alpha = 0$ in (28), corresponding to the UCM model. More details about this solution is given in [16].

The solution given by equation (32) permits us to evaluate $\dfrac{\partial u}{\partial y} = u_y$ from equation (29) in the form

$$u_y = \frac{1}{Wi}\Big(\frac{\tau^{xy}}{\tau^{yy} + \frac{1}{Re\, Wi}}\Big)\Big[1 + \alpha\, Re\, Wi(\tau^{xx} + \tau^{yy})\Big] \tag{33}$$

which introduced into equation (30), produces

$$\Big\{2\Big(\frac{(\tau^{xy})^2}{\tau^{yy} + \frac{1}{Re\, Wi}}\Big)\Big[1 + \alpha\, Re\, Wi(\tau^{xx} + \tau^{yy})\Big]\Big\} - \Big\{\tau^{xx} + \alpha\, Re\, Wi[(\tau^{xy})^2 + (\tau^{xx})^2]\Big\} = 0. \tag{34}$$

This equation can be written as a second order algebraic equation for τ^{xx} which has 2 solutions. The solution chosen for τ^{xx} is one that gives a positive first normal stress difference ($N_1 = \tau^{xx} - \tau^{yy} > 0$), in the middle of the channel and is given by

$$\tau^{xx} = \frac{-B - \sqrt{B^2 - 4AC}}{2A} \tag{35}$$

where

$$A = -\alpha\, Wi\, Re, \; B = 2\big(\tau^{xy}\big)^2 \left[\frac{\alpha\, Wi\, Re}{\tau^{yy} + \frac{1}{Wi\, Re}}\right] - 1, \; C = (\tau^{xy})^2 \left[\frac{2}{\tau^{yy} + \frac{1}{Wi\, Re}}\big(1 + \alpha\, Wi\, Re\tau^{yy}\big) - \alpha\, Wi\, Re\right]$$

Therefore, τ^{xy} and τ^{yy} are computed from (31) and (32) while τ^{xx} is obtained from (35) and finally, u_y is evaluated using (33). However, these solutions depend on the value of p_x which is calculated in the next section.

8.1   Calculation of p_x – JONATHAN COULD PLEASE DESCRIBE HOW PX IS OBTAINED

To evaluate equations (31)-(35), the value of p_x is required. It is obtained as follows: at the channel entrance, a Newtonian profile $u_{\text{inf}}(y)$ is imposed which gives $\int_0^1 u_{\text{inf}}(y)dy = 2/3$ so the Giesekus solution $u(y)$ must also provide $\int_0^1 u(y)dy = 2/3$. Using integration by-parts and the no-slip condition for $u(y)$, yields the following equation

$$\int_0^1 yu_y dy + \frac{2}{3} = 0. \tag{36}$$

The expressions (28)–(30) readily give

$$\tau^{yy} = \frac{1}{2\alpha ReWi}\left(-1 + \sqrt{1 - 4\alpha^2 Re^2 Wi^2(\tau^{xy})^2}\right), \tag{37}$$

$$\tau^{xx} = \frac{u_y(1 + ReWi\tau^{yy})}{\alpha Re^2 Wi\tau^{xy}} - \frac{(1 + \alpha ReWi\tau^{yy})}{\alpha ReWi}, \tag{38}$$

$$u_y = 2\alpha Re\tau^{xy}\frac{\left(1 + (2\alpha - 1)\sqrt{1 - 4\alpha^2 Re^2 Wi^2(\tau^{xy})^2}\right)}{\left(2\alpha - 1 + \sqrt{1 - 4\alpha^2 Re^2 W_i^2(\tau^{xy})^2}\right)^2}. \tag{39}$$

These equations reproduce those presented in [16], where (37) follows from (28), (38) from (29), whilst (39) arises from eliminating τ^{xx} between (29) and (30) and using (37). The sign choices have been chosen so that the expressions reduce to those for the UCM model when $\alpha = 0$.

Equation (31) relates the shear stress and pressure gradient p_x in the direction of flow, which is determined using the volume flux relationship (36). The integral in (36) may be evaluated explicitly

34

as follows. Using (39), we have

$$\int_0^1 y u_y dy = -\frac{2}{p_x^2} \int_0^{-\frac{p_x}{2}} \tau^{xy} u_y d\tau^{xy} = \frac{1}{2p_x^2 \alpha^2 Re^2 Wi^3} \int_{\phi-a}^{1-a} \frac{(z+a)}{z^2}(1-a(z+a))(1-(z+a)^2)^{\frac{1}{2}} dz,$$
(40)

where $z = 2\alpha - 1 + \sqrt{1 - 4\alpha^2 Re^2 Wi^2 (\tau^{xy})^2}$ with

$$a = 1 - 2\alpha, \qquad \phi = \sqrt{1 - \alpha^2 Re^2 Wi^2 p_x^2}.$$
(41)

Explicitly evaluating the quadrature in (40) and using (36) we obtain the following transcendental equation to determine p_x,

$$-\frac{4}{3}\alpha^2 Re^2 Wi^3 p_x^2 = 2(3a^2 - 1)\sqrt{\alpha(1-\alpha)} \ln \left(\frac{1 - a\phi + 2\sqrt{\alpha(1-\alpha)(1-\phi^2)}}{\phi - a} \right)$$
$$+ \frac{a}{a-\phi}(1-\phi^2)^{\frac{3}{2}} + \sqrt{1-\phi^2}\left(1 - 3a^2 - \frac{3}{2}a\phi\right) + a\left(3a^2 - \frac{5}{2}\right)\left(\sin^{-1}\phi - \frac{\pi}{2}\right).$$
(42)

This expression has not been previously noted in the literature. In the particular case $\alpha = 1/2$, (42) reduces to

$$\frac{1}{3}Re^2 Wi^3 p_x^2 - \frac{1}{2}\ln\left(\frac{1 + \frac{ReWi\, p_x}{2}}{1 - \frac{ReWi\, p_x}{2}}\right) + \frac{1}{2}ReWi\, p_x = 0,$$
(43)

which reproduces the expression of Yoo and Choi (1989) in our case (allowing for notational differences with $Re\, p_x = 2c_1$, their channel width being double and a different volume flux).

	$\alpha = 0$	$\alpha = 0.1$	$\alpha = 0.2$	$\alpha = 0.3$	$\alpha = 0.4$	$\alpha = 0.5$
Wi=0	-8.000000	-8.000000	-8.000000	-8.000000	-8.000000	-8.000000
Wi=0.2	-8.000000	-7.300155	-6.855619	-6.539274	-6.299874	-6.111361
Wi=0.4	-8.000000	-6.115756	-5.329620	-4.838947	-4.478883	-4.183502
Wi=0.6	-8.000000	-5.128988	-4.260858	-3.751357	-3.381857	-3.073223
Wi=0.8	-8.000000	-4.384128	-3.528613	-3.043154	-2.693575	-2.399257
Wi=1	-8.000000	-3.818926	-3.005257	-2.553329	-2.229699	-1.956402

Table 6: Numerical values of p_x for selected Wi and α with $Re = 1$. Upper value in each cell is obtained from the transcendental equation (42), whilst the lower value is from the full numerical scheme.

References

[1] L. Ferrás, M. Nóbrega; F. T. Pinho, Slip flows of newtonian and viscoelastic fluids in a 4:1 contraction. *J. Non-Newt. Fluid Mech.*, **214** (2014), 28-37.

[2] M. A. Alves, P. J. Oliveira, T. T. Pinho, Benchmark solutions for the flow of oldroyd-b and ptt fluids in planar contractions, *J. Non-Newt. Fluid Mech.*, **110** (2003), 45-75.

[3] M. Alves, P. Oliveira, F. T. Pinho, A convergent and universally bounded interpolation scheme for the treatment of advection, *Int. J. Num. Meth. Fluids*, **41** (2003), 47-75.

[4] H. Mokarizadeh, M. Asgharian, A. Raisi, Heat transfer in Couette-Poiseuille flow between parallel plates of the Giesekus viscoelastic fluid, *J. Non-Newt. Fluid Mech.*, **196** (2013), 95-101.

[5] V. Delvaux, M. J. Crochet, Numerical simulationof delatyed die swell, *Rheol. Acta*, **29** (1990), 1-10.

[6] J. Joie, D. Graebling, Numerical simulation of polymer flows using non-conforming finite elements, Comput. Fluids, **79** (2013), 178-189.

[7] Y. Mu, G. Zhao, A.Mokarizadeh-2013 Chen, X. Wu, Modelling and simulation of three-dimensional extrusion swelling of viscoelastic fluids with PTT, Giesekus and FENE-P constitutive models, *Int. J. Num. Meth. Fluids*, **72** (2013), 846-863.

[8] Wilco M.H. Verbeeten, GWM Peters, FPT Baaijens, Viscoelastic analysis of complex polymer melt flows using the eXtended Pom-Pom model, Journal of Non-Newtonian Fluid Mechanics Volume 108, Issues 1?3, 30 December 2002, Pages 301?326.

[9] MA Fontelos, J Li , On the evolution and rupture of filaments in Giesekus and FENE models *J. Non-Newt. Fluid Mech.* (2004), **118**, 1-16.

[10] A Raisi, M Mirzazadeh, AS Dehnavi, F Rashidi, An approximate solution for the Couette-Poiseuille flow of the Giesekus model between parallel plates - Rheologica Acta, 2008 - Springer

[11] A. Kate, Gurnon, N. J. Wagner, Large Amplitude Oscillatory shear (LAOS) measuments to obtains constitutive equation model parameters: Giesekus model of banding and nonbanding wormlike micelles, J. Rheology, vol. 56, 2012,

[12] G. S. Paulo, M. F. Tomé, S. McKee, A marker-and-cell approach to viscoelastic free surface flows using the PTT model, *J. Non-Newt. Fluid Mech.*, **147** (2007), 149-174.

[13] M. F. Tomé, G. S. Paulo, M. A. Alves, F. T. Pinho, Numerical Solution of the PTT constitutive equation for three-dimensional free surface flows, *J. Non-Newt. Fluid Mech.*, **165** (2010), 247-262.

[14] Tanner-1970

[15] H. Giesekus, A simple constitutive equation for polymer fluids based on the concept of deformation-dependent tensorial mobility, *J. Non-Newt. Fluid Mech.*, **11** (1982), 69-109.

[16] G. Schleiniger e R. J. Weinacht, Steady Poiseuille flows for a Giesekus fluid, *J. Non-Newt. Fluid Mech.*, **40** (1991), 79-102.

[17] Y. Mu, G. Zhao, A. Chen e X. Wu, Modelling and simulation of three-dimensional extrusion swelling of viscoelastic fluids with PTT, Giesekus and FENE-P constitutive models, *Int. J. Num. Meth. Fluids*, **72** (2013), 846-863.

[18] S.-C. Xue, R.I. Tanner, N. Phan-Thien, Numerical modelling of transient viscoelastic flows, *J. Non-Newt. Fluid Mech.*, **123** (2004), 33-58.

[19] Wilco M.H. Verbeeten, Gerrit W.M. Peters, Frank P.T. Baaijens, Numerical simulations of the planar contraction flow for a polyethylene melt using the XPP model, *J. Non-Newt. Fluid Mech.* **117**, (2004), 73-84.

[20] A.M. Afonso, M.A. Alves, F.T. Pinho, Purely elastic instabilities in three-dimensional cross-slot geometries, *J. Non-Newt. Fluid Mech.*, **165** (2010), 743-751.

[21] Xiaoyang Xu, Jie Ouyang, Tao Jiang, Qiang Li, Numerical simulation of 3D-unsteady viscoelastic free surface flows by improved smoothed particle hydrodynamics method, *J. Non-Newt. Fluid Mech.*, **177-178**, (2012), 109-120.

[22] Helen J. Wilson, Michael Renardy, Yuriko Renardy, Structure of the spectrum in zero Reynolds number shear flow of the UCM and Oldroyd-B liquids Original Research Article Journal of Non-Newtonian Fluid Mechanics, Volume 80, 1 January 1999, Pages 251-268

[23] J.D. Evans, D.N. Sibley, The UCM limit of the PTT equations at a re-entrant corner Journal of Non-Newtonian Fluid Mechanics, Volume 165, November 2010, Pages 1543-1549 J.D. Evans, D.N. Sibley

[24] R.J. Poole, F.T. Pinho, M.A. Alves, P.J. Oliveira The effect of expansion ratio for creeping expansion flows of UCM fluids Original Research Article Journal of Non-Newtonian Fluid Mechanics, Volume 163, November 2009, Pages 35-44

[25] R.J. Poole, A. Lindner, M.A. Alves, Viscoelastic secondary flows in serpentine channels Original Research Article Journal of Non-Newtonian Fluid Mechanics, Volume 201, November 2013, Pages 10-16

[26] J.D. Evans, Re-entrant corner flows of UCM fluids: The Cartesian stress basis Original Research Article Journal of Non-Newtonian Fluid Mechanics, Volume 150, 14 April 2008, Pages 116-138 J.D. Evans

[27] Jie Peng, Ke-Qin Zhu, Instability of the interface in co-extrusion flow of two UCM fluids in the presence of surfactant Original Research Article Journal of Non-Newtonian Fluid Mechanics, Volume 166, January 2011, Pages 152-163

[28] C.M. Oishi, F.P. Martins, M.F. Tomé, J.A. Cuminato, S. McKee, Numerical solution of the eXtended Pom-Pom model for viscoelastic free surface flows Original Research Article Journal of Non-Newtonian Fluid Mechanics, Volume 166, February 2011, Pages 165-179

[29] G.S. Paulo, C.M. Oishi, M.F. Tomé, M.A. Alves, F.T. Pinho, Numerical solution of the FENE-CR model in complex flows Original Research Article Journal of Non-Newtonian Fluid Mechanics, Volume 204, February 2014, Pages 50-61

[30] Jonathan D. Evans, Thomas Hagen, Viscoelastic sink flow in a wedge for the UCM and Oldroyd-B models Original Research Article Journal of Non-Newtonian Fluid Mechanics, Volume 154, September 2008, Pages 39-46

[31] D.O.A. Cruz, F.T. Pinho, Analytical solution of steady 2D wall-free extensional flows of UCM fluids Original Research Article Journal of Non-Newtonian Fluid Mechanics, In Press, Accepted Manuscript, Available online 24 June 2015

[32] N.J. Inkson, T.N. Phillips, R.G.M. van Os, Numerical simulation of flow past a cylinder using models of XPP type Original Research Article Journal of Non-Newtonian Fluid Mechanics, Volume 156, January 2009, Pages 7-20

[33] R.A. Figueiredo, C.M. Oishi, J.A. Cuminato, M.A. Alves, Three-dimensional transient complex free surface flows: Numerical simulation of XPP fluid Original Research Article Journal of Non-Newtonian Fluid Mechanics, Volume 195, May 2013, Pages 88-98

[34] I. Sirakov, A. Ainser, M. Haouche, J. Guillet, Three-dimensional numerical simulation of viscoelastic contraction flows using the Pom-Pom differential constitutive model, Original Research Article Journal of Non-Newtonian Fluid Mechanics, Volume 126, 10 March 2005, Pages 163-173

[35] M. Ellero, R.I. Tanner, SPH simulations of transient viscoelastic flows at low Reynolds number Original Research Article Journal of Non-Newtonian Fluid Mechanics, Volume 132, 15 December 2005, Pages 61-72

[36] R.J. Poole, M.A. Alves, P.J. Oliveira, F.T. Pinho, Plane sudden expansion flows of viscoelastic liquids Original Research Article Journal of Non-Newtonian Fluid Mechanics, Volume 146, 25 October 2007, Pages 79-91

[37] Bo Yu, Yasuo Kawaguchi, Direct numerical simulation of viscoelastic drag-reducing flow: a faithful finite difference method Original Research Article Journal of Non-Newtonian Fluid Mechanics, Volume 116, 10 January 2004, Pages 431-466

[38] S.C Xue, N Phan-Thien, R.I Tanner, Fully three-dimensional, time-dependent numerical simulations of Newtonian and viscoelastic swirling flows in a confined cylinder: Part I. Method and steady flows Original Research Article Journal of Non-Newtonian Fluid Mechanics, Volume 87, 15 November 1999, Pages 337-367

[39] K.A. Missirlis, D. Assimacopoulos, E. Mitsoulis, A finite volume approach in the simulation of viscoelastic expansion flows Original Research Article Journal of Non-Newtonian Fluid Mechanics, Volume 78, 1 August 1998, Pages 91-118

[40] Joseph Rosenberg, Roland Keunings, Numerical integration of differential viscoelastic models Original Research Article Journal of Non-Newtonian Fluid Mechanics, Volume 39, 1991, Pages 269-290

[41] Daulet Izbassarov, Metin Muradoglu, A front-tracking method for computational modeling of viscoelastic two-phase flow systems Original Research Article Journal of Non-Newtonian Fluid Mechanics, Volume 223, September 2015, Pages 122-140
****
****

[42] G. S. Paulo, M. F. Tomé, S. McKee, A marker-and-cell approach to viscoelastic free surface flows using the PTT model, Journal of Non-Newtonian Fluid Mechanics, zbf 147 (2007), 149-174.

[43] International Journal for Numerical Methods in Fluids Volume 66, Issue 3, 30 May 2011, Pages 324-344 Convected level set method for the numerical simulation of fluid buckling Ville, L. , Silva, L., Coupez, T.

[44]

[45]

[46]

[47] Maleki2004

[48] Journal of Non-Newtonian Fluid Mechanics, Volume 166, Issue 19-20, October 2011, Pages 1100-1115, Numerical simulations of mounding and submerging flows of shear-thinning jets impinging in a container (Article) Roberts, S.A., Rao, R.R.

[49] Physics of Fluids Volume 26, Issue 2, 4 February 2014, Article number 024101 Liquid supercoiling (Article) Habibi, M., Hosseini, S.H. , Khatami, M.H., Ribe, N.M.

[50] Journal of Non-Newtonian Fluid Mechanics Volume 202, December 2013, Pages 54-71 A SPH-based particle method for simulating 3D transient free surface flows of branched polymer melts (Article) Xu, X., Ouyang, J.

[51] Brazilian Symposium of Computer Graphic and Image Processing 1 October 2014, Article number 6915291, Pages 65-72 2014 27th SIBGRAPI Conference on Graphics, Patterns and Images, SIBGRAPI 2014; Rio de Janeiro; Brazil; 27 August 2014 through 30 August 2014; Category numberE5316; Code 108100 SPH fluids for viscous jet buckling (Conference Paper) De Souza Andrade, L.F.a, Sandim, M., Petronetto, F., Pagliosa, P., Paiva, A.

[52] Physics of Fluids Volume 25, Issue 4, 4 April 2013, Article number 043102 Buckling of a thin, viscous film in an axisymmetric geometry (Article) Bhattacharya, S., Craster, R.V., Flynn, M.R.

[53] Journal of Non-Newtonian Fluid Mechanics Volume 195, May 2013, Pages 88-98 Three-dimensional transient complex free surface flows: Numerical simulation of XPP fluid (Article) Figueiredo, R.A. , Oishi, C.M. , Cuminato, J.A. , Alves, M.A.

[54] M. Aboubacar e M. F. Webster, A cell-vertex finite volume/element method on triangles for abrupt contraction viscoelastic flows, Journal of Non-Newtonian Fluid Mechanics, **98** (2001), 83-106.

[55] M. A. Alves, P. J. Oliveira e F. T. Pinho, Benchmark solutions for the flow of Oldroyd-B and PTT fluids in planar contractions, Journal of Non-Newtonian Fluid Mechanics, **110** (2003), 45-75.

[56] A. A. Amsden e F. H. Harlow, A simplified mac technique for incompressible fluid flow calculations, Journal of Computational Physics, **6** (1970), 322-325.

[57] M. S. B. Araujo, Extensão de GENSMAC para escoamentos de fluidos governados pelos modelos integrais Maxwell e K-BKZ, PhD thesis, Universidade de São Paulo, Instituto de Ciências Matemáticas e Computação, São Carlos, 2006.

[58] J. Azaiez, R. Guénette e A. Aït-Kadi, Numerical simulation of viscoelastic flows through a planar contraction, Journal of Non-Newtonian Fluid Mechanics, **62** (1996), 253-277.

[59] G. K. Batchelor, An Introduction to Fluid Dynamics. Cambridge University Press, 1967.

[60] D. V. Boger, D. Hur, R. Binnington, Further observations of elastic effects in tubular entry flows, Journal of Non-Newtonian Fluid Mechanics, **20** (1986), 31-49.

[61] H. C. Choi, J. H. Song, J. Y. Yoo, Numerical simulation of the planar contraction flow of a Giesekus fluid, Journal of Non-Newtonian Fluid Mechanics, **29** (1988), 347-379.

[62] A. J. Chorin, A numerical method for solving incompressible viscous flow problems, Journal of Computational Physics, **2** (1967), 12-26.

[63] A. J. Chorin, Numerical solution of the Navier-Stokes equations, Mathematics of Computation, **22** (1968), 745-762.

[64] A. J. Chorin e J. E. Marsden, A mathematical introduction to fluid mechanics. Springer, 2000.

[65] J. O. Cruickshank, Low-reynolds-number instabilities in stagnating jet flows, Journal of Fluid Mechanics, **193** (1988), 111-127.

[66] J. O. Cruickshank e B. R. Munson, Viscous-fluid buckling of plane axisymmetric jets, Journal of Fluid Mechanics, **113** (1981), 221-239.

[67] V. Delvaux e M. J. Crochet, Numerical simulation of delayed die swell, Rheologica Acta, **29** (1990), 1-10.

[68] L. L. Ferrás, A. M. Afonso, M. A. Alves, J. M. Nóbrega, O. S. Carneiro e F. T. Pinho, Slip flows of Newtonian and viscoelastic fluids in a 4:1 contraction, Journal of Non-Newtonian Fluid Mechanics, **214** (2014), 28-37.

[69] F. H. Harlow e J. E. Welch, Numerical calculation of time-dependent viscous incompressible flow of fluid with free surface, Physics Fluids, **8** (1965), 2182-2189.

[70] W. V. D. Hodge, The theory and applications of harmonic integrals, Cambridge University Press, Cambridge.

[71] J. Joie e D. Graebling, Numerical simulation of polymer flows using non-conforming finite elements, Computers and Fluids, **79** (2013), 178-189.

[72] O. A. Ladyzhenskaja, The mathematic theory of viscous incompressible flow, Gordon and Breach, New York.

[73] J. Oliveira e F. T. Pinho, Plane contraction flows of upper convected Maxwell and Phan-Thien-Tanner fluids as predicted by a finite-volume method, Journal of Non-Newtonian Fluid Mechanics, **88** (1999), 63-88.

[74] J. Oliveira e A. Castelo, Desenvolvimento de um Sistema de Simulação de Escoamentos de Fluidos com Superfícies Livres Bidimensionais, Dissertação de mestrado, ICMC-USP de São Carlos (2002).

[75] A. Oztekin, R. A. Brown e G. H. McKinley, Quantitative prediction of the viscoelastic instability in cone-and-plate flow of a Boger fluid using a multi-mode Giesekus model, Journal of Non-Newtonian Fluid Mechanics, **54** (1994), 351-377.

[76] D. Rajagopalan, R. C. Armstrong e R. A. Brown, Finite element methods for calculation of steady viscoelastic flow using constitutive equations with a Newtonian viscosity, Journal of Non-Newtonian Fluid Mechanics, **36** (1990), 159-192.

[77] M. F. Tomé, S. McKee, GENSMAC: A computational marker and cell method for free surface flows in general domains, Journal of Computational Physics, **110** (1994), 171-186.

[78] M. F. Tomé, Numercial simulation of viscous flow: Buckling of planar jets, International Journal for Numerical Methods in Fluids, **29** (1999), 705-718.

[79] M. F. Tomé, S. McKee, L. Barratt, D. Jarvis e A. Patrick, An experimental and numerical investigation of container filling with viscous liquids, International Journal for Numerical Methods in Fluids, **33** (1999), 1333-1353.

[80] M. F. Tomé, A. Castelo, C. N. L. César, S. McKee e J. A. Cuminato, Freeflow: an integrated simulation system for three-dimensional free surface flows, Computing and Visualization in Science, **2** (2000), 199-210.

[81] M. F. Tomé, N. Mangiavacchi, J. A. Cuminato, A. Castelo e S. McKee, A finite difference technique for simulating unsteady viscoelastic free surface flows, Journal of Non-Newtonian Fluid Mechanics, **106** (2002), 61-106.

[82] Murilo F. Tomé, José L. Doricio, José A. Cuminato, Antonio Castelo, Sean McKee, Solving viscoelastic free surface flow of a second order fluid using a marker-and-cell method approach , *International Journal for Numerical Methods in Fluids*, Vol. 53, pp. 599-627 (2007).

[83] M. F. Tomé, A. Castelo, V. G. Ferreira e S. McKee, A finite difference technique for solving the Oldroyd-B model for 3D-unsteady free surface flows, Journal of Non-Newtonian Fluid Mechanics, **154** (2008), 159-192.

[84] M. F. Tomé, M. S. B. Araujo, M. A. Alves e F. T. Pinho, Numerical simulation of viscoelastic flows using integral models: a finite difference approach, Journal of Computational Physics, **227** (2008), 4207-4243.

[85] M. F. Tomé, G. S. Paulo, M. A. Alves e F. T. Pinho, Numerical solution of the PTT constitutive equation for three-dimensional free surface flows, Journal of Non-Newtonian Fluid Mechanics, **165** (2010), 247-262.

[86] M. F. Tomé, A. Castelo, A. M. Afonso, M. A. Alves e F. T. Pinho, Application of the log-conformation tensor to three-dimensional time-dependent free surface flows, Journal of Non-Newtonian Fluid Mechanics, **175-176** (2012), 44-54.

[87] A. Varonos e G. Bergeles, Development and assessment of a variable-order non-oscillatory scheme for convection term discretization, International Journal for Numerical Methods in Fluids, **26** (1998), 1-16.

[88] K. Walters e M. F. Webster, The distinctive cfd challenges of computational rheology, International Journal for Numerical Methods in Fluids, **43** (2000), 577-596.

[89] S. A. White, A. Gotsis e D. G. Baird, Review of the entry flow problem: Experimental and numerical, Journal of Non-Newtonian Fluid Mechanics, **24** (1987), 121-160.

[90] I. Dapra, G. Scarpi, Couette-Poiseulle flow of the Giesekus model between parallel plates, Rheol. Acta, **48** (2009), 117-120.

[91] Analytical solutions for channel flows of Phan-Thien-Tanner and Giesekus fluids under slip, Journal of Non-Newtonian Fluid Mechanics, **171-172** (2012), 97-105.

[92] Flow of viscoelastic fluid past a cylinder at high Weissenberg number: stabilized simulations with matrix logarithms, Journal of Non-Newtonian Fluid Mechanics, **127** (2005), 27-39.

[93] On the steady simple shear flows of the one-mode Giesekus fluid, Rheol. Acta, **28** (1989), 13-24.